

Complex Neural Network based Joint AoA and AoD Estimation for Bistatic ISAC

Salmane Naoumi, Ahmad Bazzi, Roberto Bomfin, Marwa Chafii

Abstract—Integrated sensing and communication (ISAC) in wireless systems has emerged as a promising paradigm, offering the potential for improved performance, efficient resource utilization, and mutually beneficial interactions between radar sensing and wireless communications, thereby shaping the future of wireless technologies. In this work, we present two novel methods to address the joint angle of arrival and angle of departure estimation problem for bistatic ISAC systems. Our proposed methods consist of a deep learning (DL) solution leveraging complex neural networks, in addition to a parameterized algorithm. By exploiting the estimated channel matrix and incorporating a preprocessing step consisting of a coarse timing estimation, we are able to notably reduce the input size and improve the computational efficiency. In our findings, we emphasize the remarkable potential of our DL-based approach, which demonstrates comparable performance to the parameterized method that explicitly exploits the multiple-input multiple-output (MIMO) model, while exhibiting significantly lower computational complexity.

Index Terms—Integrated sensing and communication (ISAC), bistatic radar, deep learning (DL), angle of arrival (AoA) estimation, angle of departure (AoD) estimation

I. INTRODUCTION

The advent of integrated sensing and communication (ISAC) marks a transformative breakthrough for the realm of 6G networks [1]. While radar sensing and wireless communications have traditionally progressed independently, the emergence of joint communication and sensing now brings forth a game-changing paradigm, presenting unprecedented opportunities to revolutionize spectrum efficiency, reduce hardware cost and power consumption, and redefine how networks perceive and interact with their surroundings. Given this context, ISAC has attracted significant research interest and attention from both academic and industrial sectors. Indeed, various scenarios and challenges have been explored. These include, dual-functional radar and communication (DFRC) [2], unmanned aerial vehicles [3], waveform design [4], beamforming design [5], security [6], [7], and intelligent reflecting surfaces [8], [9].

Communication-centric ISAC, which is based on the utilization of an optimized communication waveform for sensing tasks, is a promising research area that offers the potential for fruitful outcomes by leveraging transmitted communication

signals to enhance sensing capabilities. Repurposing the estimation process of channel state information provides an opportunity to accurately determine physical sensing parameters like the direction of arrival (DoA), range, and speed of targets of interest. Indeed, numerous research studies have examined and validated the utilization of bistatic radar topology in conjunction with orthogonal frequency-division multiplexing (OFDM)-based signal processing to address communication-aided sensing optimization [10]–[12]. Notably, they have explored this approach within a practical bistatic setup [13], demonstrating its effectiveness in accurately detecting and estimating target parameters such as delay and Doppler shift. Furthermore, a power budget analysis was conducted in [14] to study the behavior of communication and radar signal-to-noise ratios (SNRs) as function of distance. Nevertheless, processing the received communication signal to achieve high sensing quality remains practically challenging, as both communications and radar systems are not mutually optimized for the sensing function. Various challenges arise when designing the radar signal processing functions, including high peak-to-average power ratio [15], clutter noise, multi-path reflections, unoptimized side-lobes, and Doppler ambiguity caused by the cyclic prefix (CP) [16].

In this work, we investigate parameter estimation in a bistatic radar setup within an ISAC system, where we focus on estimating both angle of arrival (AoA) and angle of departure (AoD). Since the maximum likelihood estimator is a highly multidimensional optimization problem, which is infeasible to be realized in real-time with practical hardware resources, we propose to leverage neural networks (NNs) ability of being universal approximators, to perform this complex estimation problem with low complex optimized NN architectures. In the literature [17], the AoA and AoD estimation problem is either framed as a regression problem [18], [19] by training architectures like the multi-layer perceptron (MLP) to minimize an objective function such as the mean squared error (MSE) between estimates and true angles, or as a spectrum based sensing estimation [20], [21] where an NN is trained on hot encoded ground-truth vectors representing targets likelihoods at given angles of a discrete grid with a given cardinality. In the latter case, the network does not rely on prior knowledge of the number of targets. Instead, it is trained to output an estimated spectrum and subsequently requires an additional step for target detection to extract angle estimates from peaks, as commonly employed in conventional methodologies like MUSIC. Other DL approaches have been proposed such as a multi-stage DL [22] consisting of a multitask autoencoder and a series of parallel multi-layer classifiers. In our study, we present a novel method addressing the sensing estimation

Salmane Naoumi is with NYU Tandon School of Engineering, Brooklyn, 11201, NY (e-mail: sn3397@nyu.edu).

Roberto Bomfin is with the Engineering Division, New York University (NYU) Abu Dhabi, UAE (e-mail: rcd9059@nyu.edu).

Ahmad Bazzi and Marwa Chafii are with the Engineering Division, New York University (NYU) Abu Dhabi, UAE and NYU WIRELESS, NYU Tandon School of Engineering, Brooklyn, NY (e-mail: ahmad.bazzi@nyu.edu, marwa.chafii@nyu.edu).

problem that capitalizes on a distinct input and trains complex-valued NNs to minimize the MSE objective function on training datasets generated using the ideal system model. Moreover, we propose a parameterized algorithm that exploits the knowledge of the model to be used for benchmarking. More specifically, the parameterized 2D method estimates the AoA and AoD of the targets utilizing full knowledge of array steering vectors and OFDM sub-carrier regular structure. Although OFDM is assumed in the model, our work remains valid for any precoded OFDM modulation such as discrete Fourier transform (DFT)-spread OFDM. For comparison, the Cramér-Rao bound (CRB) is also shown. The results reveal that the DL-based solution provides a comparable estimation performance to the parameterized method, while requiring considerably less computational efforts.

The main contributions of this work are summarized as follows.

- **Novel joint AoA/AoD DL estimator.** We present a new DL technique for sensing parameter estimation, i.e. the AoAs and AoDs in an ISAC system. Departing from conventional input sources, the method utilizes the estimated channel matrix, which captures essential information regarding the sensing parameters. The DL model employs complex-valued neural networks, and includes complex convolutional and linear layers, with weights represented as complex matrices, enhancing the model's ability to accurately represent the channel matrix. The complex rectified linear unit (CReLU) is chosen as the activation function. The network structure comprises three hidden layers and a final output layer predicting the sensing parameters. Moreover, the MSE serves as the objective function during the training phase.
- **Novel design of a parameterized AoA/AoD estimator.** We develop a parameterized method for AoA/AoD estimator, which exploits the complete model knowledge, including the array geometries. The method involves transforming the received channel matrix by leveraging the uniform linear antenna (ULA) structures at transmit and receive sides into smaller channel matrices with given sub-array sizes. The method makes use of the induced Hankel structure to further compute certain eigenvalues, which aid in the AoD estimation. Regarding AoA estimation, a least squares (LS) fit is required at a later stage of the algorithm.

Furthermore, we unveil some important insights, i.e.

- Through simulations, we study the impact of training SNR on the achieved MSE performance. More specifically, the MLP architecture is trained using simulation data generated at specific SNRs, and the network's performance is evaluated on a test dataset spanning a range of given SNR values. We observe that loss curves steadily decrease during training, indicating effective learning and generalization to unseen data. Regarding overfitting, we employ a learning rate schedule. In addition, we showcase various simulation results illustrating the superior performance and potential of the proposed methods compared, and their closeness to the CRB benchmarks.

- We conduct a comprehensive computational complexity analysis of the two proposed methods, focusing on the total number of multiplications and additions required for their implementation. This analysis includes a detailed examination of the complexities associated with the DL technique, which employs architectures with three hidden layers, by counting the complexities involved in its different operations. Moreover, for the parameterized approach, we provide a breakdown of the computational complexities associated with specific blocks, such as channel estimation, coarse timing estimation, and sensing estimation. This includes highlighting the estimation overheads and detailing the total number of operations for each block. We also present the maximum likelihood criterion for the estimation problem at hand, emphasizing the significant complexity reductions achieved by both methods compared to the maximum likelihood estimator (MLE). Additionally, our simulations demonstrate that, in comparison to the parametric 2D estimation procedure, the proposed DL technique enjoys less computational complexity. For example, with 8 receive antennas, the 2D algorithm requires 6.5 times more multiplications than the DL one, which is 15.27% of the computational complexity required by the 2D algorithm for multiplications. Despite a performance degradation, especially at higher SNR values, these results highlight the significant percentage increases in computational efficiency and scalability provided by the DL design.
- We investigate the influence of antenna radiation patterns on the performance of bi-static ISAC systems. After incorporating these patterns into our system model, we explore how changes in their parameters impact the CRB. Our analysis reveals that narrower, more focused beams require higher SNRs to attain a predetermined CRB for target sensing applications. This insight emphasizes the complex interplay between antenna design choices and the performance of ISAC systems, highlighting the importance of integrating the radiation pattern characteristics to enhance the sensing accuracy in realistic applications.

The detailed structure of the following paper is given as follows. In Section II, we introduce the communication-centric ISAC system model, along with the channel estimator and coarse timing estimate used throughout the paper. Section III derives the maximum likelihood estimator of the estimation problem. In Section IV, we present our machine learning-based AoA and AoD estimator, accompanied with its computational complexity. Moreover, Section V presents our 2D parametrized estimator, along with its detailed computational complexity analysis. Section VI provides numerical results to verify our analysis before concluding the paper in Section VII.

Notation: Upper-case and lower-case boldface letters denote matrices and vectors, resp. $(\cdot)^T$, $(\cdot)^*$, $(\cdot)^H$ and $(\cdot)^\dagger$ represent the transpose, the conjugate, the transpose-conjugate, and the pseudo-inverse operators. We denote by $*$ the convolution operator. For any complex number $z \in \mathbb{C}$, the magnitude is denoted as $|z|$, and its angle is $\arg(z)$. The real part of z is denoted as $\Re(z)$, whereas the imaginary part is denoted

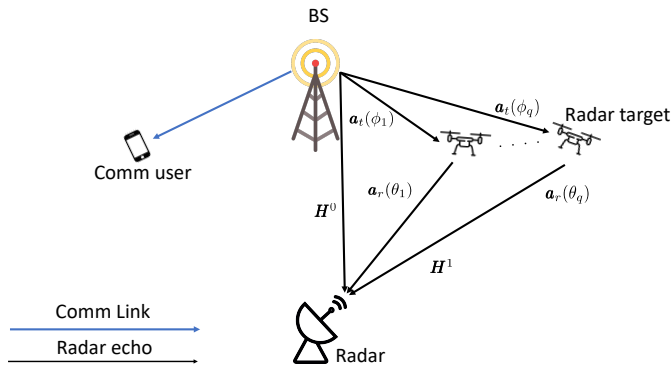


Fig. 1: An ISAC scenario composed of q targets in a bistatic fashion.

as $\Im(z)$. The ℓ_2 norm of a vector \mathbf{x} is denoted as $\|\mathbf{x}\|$. The matrices \mathbf{F} and \mathbf{I} are the Fourier and the identity matrices with appropriate dimensions, resp. For matrix indexing, the $(i, j)^{th}$ entry of matrix \mathbf{A} is denoted by $[\mathbf{A}]_{[i,j]}$ and its j^{th} column is denoted as $\mathbf{A}_{[:,j]}$. The operator \otimes is the *Kronecker* product. The big- \mathcal{O} notation is $\mathcal{O}(\cdot)$. The $\text{res}_{M,N}(\mathbf{x})$ is the reshape operator which returns an array of dimensions $M \times N$ with the same entries as the input data \mathbf{x} . Also, the operator $\text{mod}_y(x)$ denotes the remainder of the division x/y .

II. SYSTEM MODEL

Consider a base station (BS) with N_t antennas transmitting OFDM symbols in the downlink. The OFDM symbol duration, excluding the CP, is denoted as $T = \frac{1}{\Delta_f}$, where Δ_f is the sub-carrier spacing. Before expressing the transmit symbols, we describe the wireless channel related to the bistatic radar. The ISAC framework can be classified into three categories: *communication-centric*, *radar-centric*, and *joint design* [23], [24]. This paper primarily focuses on the communication-centric class of ISAC, whereby radar sensing can be considered as an "add-on" to a communication system [25]. The key objective of this design approach is to utilize communication waveforms for extracting radar information through signal processing of target echoes. On the other hand, in radar-centric design, the approach involves modulating information signaling within established radar waveforms, such as chirping [26]. The joint design category encompasses systems that are collaboratively designed from the outset to achieve a flexible balance between sensing and communication performance [27], [28]. As this paper explores a scenario where a communication signal is transmitted to each user by a BS primarily dedicated to communications, and the radar receiver utilizes the backscattered communication signal for precise estimation of target sensing parameters, the configuration of ISAC can effectively be associated to the communication-centric category. Furthermore, we note that we are using preamble knowledge based on communication standards to perform sensing tasks, hence an ISAC integration. The literature contains some work relating to communication-centric ISAC. For example, a mono-static setting of this ISAC setting has been described in [29] for orthogonal time frequency space (OTFS) digital modulation.

Moreover, a time-division duplexing (TDD) massive multiple-input, multiple-output (MIMO) system was adopted in [30], where a BS serving communication users, while profiting from the scattered signal to sense the environment. To this extent, the system model is represented in Fig. 1.

A. Bistatic Radar Channel Model

Under the simplifying assumptions of no clutter, no frequency and time offsets between the BS and the radar unit, and fixed targets, the general channel impulse response (CIR) between the n_t^{th} transmit antenna at the BS and the n_r^{th} receive antenna at the radar unit can be expressed as

$$h_{n_r, n_t}(t, \tau) = \sum_{m=0}^q \alpha_m \bar{a}_{n_r}(\theta_m) \bar{a}_{n_t}(\phi_m) \delta(\tau - \tau_m), \quad (1)$$

where $n_r = 1 \dots N_r$ and $n_t = 1 \dots N_t$ for N_r receive antennas, and N_t transmit antennas. In addition, α_m and τ_m denote the signal attenuation coefficient and delay of the m^{th} reflection, respectively, and are assumed to be time-invariant during the parameter estimation period. The function $\delta(\cdot)$ is the Dirac delta function, and q is the number of targets. Furthermore, θ_m represents the AoA between the m^{th} target and the radar unit, and ϕ_m is the AoD between the BS and the m^{th} target. Moreover, the quantity $\bar{a}_{n_t}(\phi)$ is the *actual steering coefficient* of the n_t^{th} transmit antenna at the BS towards an angle ϕ . Likewise, $\bar{a}_{n_r}(\theta)$ is the actual steering coefficient of the n_r^{th} receive antenna at the radar towards an angle θ . Typically, antennas have the capability to emit energy in specific directions, allowing for targeted radiation within a defined region of space. This is in contrast to omnidirectional antennas, which evenly perceive signals from all spatial coordinates. To quantify this, we resort to the antenna radiation pattern, which is defined as a complex function of direction, whose value gives the intensity of the radiated field in the far field area [31]. Assuming identical, but unknown, transmit antennas are used at the BS, the transmit steering vector can be defined as [32]

$$\bar{a}_{n_t}(\phi) = g_t(\phi) a_{n_t}(\phi), \quad (2)$$

where $g_t(\phi)$ is the transmit antenna radiation pattern at angle ϕ . Similarly, the receive steering vector can be also defined as

$$\bar{a}_{n_r}(\theta) = g_r(\theta) a_{n_r}(\theta), \quad (3)$$

where $g_r(\theta)$ is the receive antenna radiation pattern, also assumed to be unknown. Note that in the expressions found in equations (2) and (3), the actual transmit and receive steering vectors are written as a function of the hypothetical isotropic steering vectors, namely $a_{n_t}(\phi)$ and $a_{n_r}(\theta)$. Said differently, setting $g_t(\phi)$ (similarly $g_r(\theta)$) to unity, we coincide with the hypothetical isotropic case. Note that the first path, i.e. $m = 0$, represents the line of sight (LoS) path between the BS and the radar unit. The channel given in (1) can be expressed in the discrete frequency domain on the n^{th} sub-carrier, in matrix form, as

$$\mathbf{H}_n = \bar{\mathbf{A}}_r(\Theta) \Psi \mathbf{D}_n(\tau) \bar{\mathbf{A}}_t^T(\Phi) \in \mathbb{C}^{N_r \times N_t}, \quad (4)$$

where

$$\bar{\mathbf{A}}_t(\Phi) = [\bar{\mathbf{a}}_t(\phi_0) \quad \bar{\mathbf{a}}_t(\phi_1) \quad \dots \quad \bar{\mathbf{a}}_t(\phi_q)], \quad (5)$$

and

$$\bar{\mathbf{A}}_r(\Theta) = [\bar{\mathbf{a}}_r(\theta_0) \quad \bar{\mathbf{a}}_r(\theta_1) \quad \dots \quad \bar{\mathbf{a}}_r(\theta_q)], \quad (6)$$

are the *actual steering matrices* resulting from the AoDs between the BS-targets and the AoAs between targets-radar, respectively. Moreover, $\Psi = \text{diag}([\alpha_0 \quad \dots \quad \alpha_q])$ includes the signal attenuation coefficients. Also, $\mathbf{D}_n(\tau) = \text{diag}([c_n(\tau_0) \quad \dots \quad c_n(\tau_q)])$ is a matrix containing all delays $c_n(\tau) = e^{-j2\pi n\Delta f\tau}$. In the next sub-section, we describe the received signal in the frequency domain as seen by the radar. Using equations (2), (3), we can write the actual steering matrices in terms of their hypothetical counterparts as

$$\bar{\mathbf{A}}_t(\Phi) = \mathbf{G}_t(\Phi)\mathbf{A}_t(\Phi), \quad (7)$$

and

$$\bar{\mathbf{A}}_r(\Theta) = \mathbf{G}_r(\Theta)\mathbf{A}_r(\Theta), \quad (8)$$

where $\mathbf{G}_t(\Phi) = \text{diag}([g_t(\phi_0) \quad \dots \quad g_t(\phi_q)])$ and $\mathbf{G}_r(\Theta) = \text{diag}([g_r(\theta_0) \quad \dots \quad g_r(\theta_q)])$ are matrices arising due to the impact of the antenna radiation pattern at the arrays placed at the BS and the radar, respectively. Moreover, $\mathbf{A}_t(\Phi)$ and $\mathbf{A}_r(\Theta)$ are the hypothetical steering matrices, which are defined similar to $\bar{\mathbf{A}}_t(\Phi)$ and $\bar{\mathbf{A}}_r(\Theta)$ found in equations (5) and (6), respectively. Invoking (7) and (8) in (4) and applying the commutativity property of diagonal matrices (i.e. $\mathbf{YZ} = \mathbf{ZY}$ for any two diagonal matrices \mathbf{Y} and \mathbf{Z}), we can encapsulate the model as follows

$$\mathbf{H}_n = \mathbf{A}_r(\Theta)\mathbf{G}\mathbf{D}_n(\tau)\mathbf{A}_t^T(\Phi), \quad (9)$$

where \mathbf{G} jointly contains attenuation components, along with transmit and receive antenna radiation patterns, i.e. $\mathbf{G} = \mathbf{G}_r(\Theta)\Psi\mathbf{G}_t(\Phi)$. Note that \mathbf{G} preserves its diagonal structure, and can be expressed as $\mathbf{G} = \text{diag}([\alpha_0 g_t(\phi_0)g_r(\theta_0) \quad \dots \quad \alpha_q g_t(\phi_q)g_r(\theta_q)])$. For simplicity, we denote $\check{\alpha}_k = \alpha_k g_t(\phi_k)g_r(\theta_k)$ and treat $\check{\alpha}_k$ as an unknown quantity incorporating the channel unknown components, and the transmit/receive antenna radiation patterns.

B. Radar Signal Model

The BS transmits K OFDM signals serving communication users in the scene. The k^{th} OFDM can be expressed as

$$\mathbf{x}_k(t) = \sum_{n=1}^N \mathbf{s}_{n,k} c_n(-t) \Pi(t - kT_o), \quad \forall k = 1 \dots K, \quad (10)$$

where N is the number of active sub-carriers occupying each of the K OFDM symbols and $T_o = T + T_{CP}$ is the overall OFDM symbol duration. Moreover, $\Pi(t)$ is the windowing function. We assume an ideal rectangular function, that is

$$\Pi(t) = \begin{cases} 1, & t \in [-T_{CP}, T] \\ 0, & \text{otherwise,} \end{cases} \quad (11)$$

where T_{CP} is the CP duration, which should be greater than the maximum of propagation delays in order to guarantee a cyclic

convolution with the channel. Furthermore, $\mathbf{s}_{n,k} \in \mathbb{C}^{N_t \times 1}$ is the modulated symbol onto the n^{th} OFDM sub-carrier within the k^{th} OFDM symbol. We note that in case of precoded OFDM, $\mathbf{s}_{n,k}$ simply represents the resulting signal to be transmitted in the corresponding n^{th} sub-carrier after precoding the data symbols associated with the k^{th} transmission block. Combining (4), (10), (11) and applying fast Fourier transform (FFT), the radar unit reads the following data on the n^{th} subcarrier and k^{th} OFDM symbol,

$$\mathbf{y}_{n,k} = \mathbf{H}_n \mathbf{s}_{n,k} + \mathbf{w}_{n,k} \in \mathbb{C}^{N_r \times 1}. \quad (12)$$

The vector $\mathbf{w}_{n,k}$ is additive white Gaussian noise (AWGN) on the n^{th} sub-carrier and k^{th} symbol, with zero mean and covariance $\sigma^2 \mathbf{I}$. In this paper, we focus on a communication-centric ISAC problem, where an existing infrastructure is performing communication tasks, whereas a radar unit is installed to estimate the sensing parameters of the different targets.

C. Channel Estimation

In this sub-section, we describe the channel estimates that are used for both DL-based and parameterized methods to estimate AoA and AoD. Assuming K_P OFDM symbols occupying N_P sub-carriers each are being transmitted, and assuming that the radar unit has knowledge about the data symbols being transmitted, the channel estimation is performed according to the well-known least squares as follows

$$\bar{\mathbf{H}}_n = \mathbf{Y}_n \mathbf{S}_{P,n}^H (\mathbf{S}_{P,n} \mathbf{S}_{P,n}^H)^{-1}, \quad (13)$$

where \mathbf{Y}_n contains all pilot OFDM symbols, i.e. $\{\mathbf{y}_{n,k}\}_{k=1}^{K_P}$. Likewise, $\mathbf{S}_{P,n}$ contains the known pilot information, $\{\mathbf{s}_{n,k}\}_{k=1}^{K_P}$. Note that $\bar{\mathbf{H}}_n = \mathbf{H}_n + \mathbf{W}_{P,n} \mathbf{S}_{P,n}^H (\mathbf{S}_{P,n} \mathbf{S}_{P,n}^H)^{-1}$. It is more convenient to express channel state information (CSI) estimates as follows

$$\bar{\mathbf{H}} = [\text{vec}(\bar{\mathbf{H}}_1) \quad \text{vec}(\bar{\mathbf{H}}_2) \quad \dots \quad \text{vec}(\bar{\mathbf{H}}_{N_P})], \quad (14)$$

where $\bar{\mathbf{H}} \in \mathbb{C}^{N_t N_r \times N_P}$ contains the frequency domain channel in its rows for all combinations of transmit/receive antenna pairs. We can express $\bar{\mathbf{H}}$ in terms of its true and noise counterparts as

$$\bar{\mathbf{H}} = \mathbf{H} + \bar{\mathbf{W}}, \quad (15)$$

where $\mathbf{H} = [\text{vec}(\mathbf{H}_1) \quad \dots \quad \text{vec}(\mathbf{H}_{N_P})]$ and

$$\bar{\mathbf{W}} = [\text{vec}(\mathbf{W}_{P,1} \mathbf{S}_{P,1}^\dagger) \quad \dots \quad \text{vec}(\mathbf{W}_{P,N_P} \mathbf{S}_{P,N_P}^\dagger)], \quad (16)$$

where, for short, $\mathbf{S}_{P,n}^\dagger$ stands for the pseudo-inverse of $\mathbf{S}_{P,n}$, i.e. $\mathbf{S}_{P,n}^\dagger = \mathbf{S}_{P,n}^H (\mathbf{S}_{P,n} \mathbf{S}_{P,n}^H)^{-1}$ for all n .

D. Coarse Timing Estimation

The size of the channel estimation matrix in (14) can be reduced in order to estimate AoA and AoD, such that the input size of the machine learning (ML) algorithm is decreased. Since each row of $\bar{\mathbf{H}}$ in (14) represents the frequency domain channel over a given transmit and receive antenna pair, we can take the IFFT of (14) over its rows, and find the peaks corresponding to the time delay of a target reflection, which

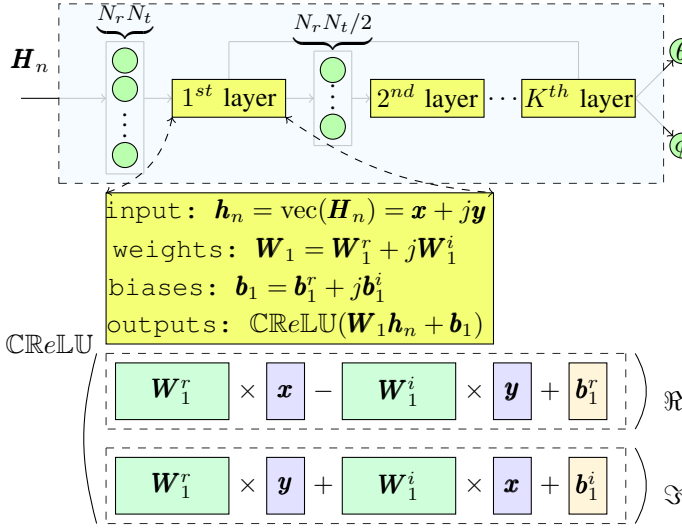


Fig. 2: Architecture of the proposed feed-forward NN composed of complex-valued linear layers and $\mathbb{C}\text{ReLU}$ activation functions. The channel matrix at each peak is used to compute the corresponding AoA and AoD.

can be interpreted as a coarse timing estimation for the delay as a multiple of the sampling time. Notice that the AoA and AoD have a direct relation with the phase of the peaks in the time domain, thus, a matrix of size $N_t \times N_r$ with the peaks can be used to estimate these parameters instead of the larger matrix of (14). This method is briefly shown in the following. The inverse fast Fourier transforms (IFFTs) per transmit/receive antenna pairs is performed as

$$\bar{\mathbf{h}}_n = \text{IFFT}(\bar{\mathbf{H}}_{[n,:]}^T) = \mathbf{F}^H \bar{\mathbf{H}}_{[n,:]}^T, \quad (17)$$

$\forall n = 1 \dots N_r N_t$. Then, the task is basically to find the indexes k corresponding to the q most likely peaks over all antenna pairs $|\bar{\mathbf{h}}_{n[k]}|$ from $\bar{\mathbf{h}}_n = [\bar{\mathbf{h}}_{n[1]} \dots \bar{\mathbf{h}}_{n[N_P]}] \in \mathbb{C}^{N_P}$, which are defined as

$$k \in \{\hat{i}_1, \dots, \hat{i}_q\}, \quad (18)$$

and are found by analyzing the peaks of all $N_t N_r$ antenna pairs. Note that a coarse estimation of the times of arrival (ToAs) is obtained by scaling the indices as $\hat{\tau}_k = \frac{1}{N_P \Delta_f} \hat{i}_k$, $\forall k = 1 \dots q$. Two extreme cases are discussed: (i) In the well-separated case, i.e. when all i_k s are distinct ($i_1 \neq i_2 \neq \dots \neq i_q$), it is easily verified that the i_k -th row of $\mathbf{F}^H \bar{\mathbf{H}}^T$ is the only row that contains information about θ_k and ϕ_k . (ii) In the other extreme case where all τ_k 's arrive within the same time index, which leads to $i \triangleq i_1 = i_2 = \dots = i_q$, then the i^{th} row $\mathbf{F}^H \bar{\mathbf{H}}^T$ is the only row that contains all AoA and AoD information. To accommodate for the worst-case, we describe an algorithm able to discriminate between all the angles of arrival (AoAs) and angles of departure (AoDs). In that case, the i^{th} row of $\mathbf{F}^H \bar{\mathbf{H}}^T$ can be reshaped as

$$\hat{\mathbf{H}} = \text{res}_{N_r, N_t}[(\mathbf{F}^H)_{[i,:]} \bar{\mathbf{H}}^T] = \mathbf{A}_r(\Theta) \mathbf{G} \mathbf{A}_t^T(\Phi) + \hat{\mathbf{W}}. \quad (19)$$

Note that $\hat{\mathbf{W}} = \text{res}_{N_r, N_t}[(\mathbf{F}^H)_{[i,:]} \bar{\mathbf{W}}^T]$ and $\bar{\mathbf{W}}$ is defined in (16). Note that for the well-separated case, the i_k -th row of

$\mathbf{F}^H \bar{\mathbf{H}}^T$ would be $\alpha_k g_t(\phi_k) g_r(\theta_k) \mathbf{a}_r(\theta_k) \mathbf{a}_t^T(\phi_k) + \hat{\mathbf{W}}_k$, i.e. a special case of (19). An intermediate case can also be discussed where some paths, say $p < q$, arrive within the same bin. In that case, the corresponding row is also cast as (19), however, the dimension q would be replaced with p . Note that both, the channel estimation and the coarse timing estimation, are indeed classical approaches in the context of communications. For instance, the channel estimation procedure corresponds to the well-established least-squares. In addition, the coarse timing estimation process can be used for synchronizing communication frames. Based on this, the primary objective is to demonstrate that sensing can be effectively achieved through the application of familiar preprocessing techniques. These techniques are widely recognized within the research community and are characterized by their ease of implementation.

III. THE MAXIMUM LIKELIHOOD ESTIMATOR

In this section, we describe the deterministic MLE criterion for the observed data in (12). The deterministic MLE regards the sample functions as unknown deterministic sequences, rather than random processes. To this end, we can express the joint density function of the data as follows

$$f(\mathbf{Y}) = \prod_{n=1}^{N_P} \prod_{k=1}^{K_P} \frac{1}{\pi \det(\sigma^2 \mathbf{I})} \exp\left(-\frac{1}{\sigma^2} \|\mathbf{y}_{n,k} - \mathbf{H}_n \mathbf{s}_{n,k}\|^2\right),$$

where the k^{th} column of \mathbf{Y} is $\mathbf{Y}_{[:,k]} = [\mathbf{y}_{1,k} \dots \mathbf{y}_{N_P,k}]^T$. Note that $f(\mathbf{Y})$ is conditioned over the pilots $\mathbf{s}_{n,k}$, σ^2 , $\check{\boldsymbol{\alpha}} = [\check{\alpha}_0 \dots \check{\alpha}_q]$, Θ , Φ and this dependency has been omitted for sake of compact notation. We express the log-likelihood as

$$\mathcal{L} \triangleq \log f(\mathbf{Y}) = g(\sigma^2) - \frac{1}{\sigma^2} \sum_{n=1}^{N_P} \sum_{k=1}^{K_P} \|\mathbf{y}_{n,k} - \mathbf{H}_n \mathbf{s}_{n,k}\|^2,$$

where g is only a function of σ^2 . As we are interested in the sensing parameters, we can re-write the MLE as

$$\arg \min_{\check{\boldsymbol{\alpha}}, \Theta, \Phi, \boldsymbol{\tau}} \left\| \mathbf{Y} - [\mathbf{I}_{N_P} \otimes \mathbf{A}_r(\Theta) \mathbf{G}] \mathbf{D}(\boldsymbol{\tau}) [\mathbf{I}_{N_P} \otimes \mathbf{A}_t^T(\Phi)] \mathcal{S} \right\|^2 \quad (20)$$

where the k^{th} column of \mathcal{S} is $\mathcal{S}_{[:,k]} = [\mathbf{s}_{1,k} \dots \mathbf{s}_{N_P,k}]^T$. Also, $\mathbf{D}(\boldsymbol{\tau}) = \text{diag}(\mathbf{D}_1(\boldsymbol{\tau}), \dots, \mathbf{D}_{N_P}(\boldsymbol{\tau}))$. Note that to obtain the AoA and AoD information, one has to exhaustively solve the multi-dimensional optimization problem in (20), which involves a $5q$ -dimensional search. Therefore, we resort to machine learning and parameterized methods to estimate the sensing parameters. More specifically, a grid search on the MLE criterion in (20) would cost $\mathcal{O}(G_\tau^q G_\theta^q G_\phi^q G_\alpha^{2q} (N_r N_P q^2 N_P^3 N_t + N_r N_P^2 N_P K_P))$, where $G_\tau, G_\theta, G_\phi, G_\alpha$ are the grid sizes of the time of arrival (ToA), AoA, AoD and path gains, respectively.

IV. MACHINE LEARNING-BASED AOA AND AOD ESTIMATION

While most of the reviewed literature [17]–[19] uses the receive matrix¹, the known pilot information $\mathcal{S}_{P,n}$ or their

¹In our case it corresponds to \mathbf{Y}_n containing all OFDM symbols.

covariance matrix as input, we exploit here the estimated channel matrix to extract from the IFFT over its rows a matrix $\widehat{\mathbf{H}}_k$ of reduced size $N_t \times N_r$ containing all the information about θ_k and ϕ_k , as described in Section II-D. As for the deep network design, a straightforward approach is to use an MLP and preprocess the complex-valued input to an adequate input tensor, e.g. by concatenating the real, imaginary and complex argument parts of the input, as done in [21], i.e.

$$\widehat{\mathbf{I}}_k = \left[\Im \left\{ \widehat{\mathbf{H}}_k \right\}; \arg \left\{ \widehat{\mathbf{H}}_k \right\}; \Re \left\{ \widehat{\mathbf{H}}_k \right\} \right] \in \mathbb{R}^{N_t \times N_r \times 3}. \quad (21)$$

However, in our work, we leverage complex-valued NNs [33], inspired by recent findings indicating that complex numbers possess a richer representational capacity and attractive properties. This choice is particularly relevant due to the inherent complex-value operations involved in modeling communication systems. Hence, we use complex convolutional and linear layers as fundamental building blocks for our networks. Indeed, the weights of the linear layers and convolution filters are specifically represented as complex matrices $\mathbf{W} = \mathbf{W}^r + j\mathbf{W}^i$. This approach allows us to effectively leverage the inherent complex-valued operations within these layers, enabling more expressive and accurate modeling capabilities. For example, when performing the equivalent conventional real-valued convolution in the complex domain with a complex vector $\mathbf{h} = \mathbf{x} + j\mathbf{y}$, we have

$$\mathbf{W} * \mathbf{h} = (\mathbf{W}^r * \mathbf{x} - \mathbf{W}^i * \mathbf{y}) + j(\mathbf{W}^i * \mathbf{x} + \mathbf{W}^r * \mathbf{y}). \quad (22)$$

This is due to the distributive property of the convolution operator. Using matrix notation to depict the real and imaginary components of the convolution operation, we have

$$\begin{bmatrix} \Re(\mathbf{W} * \mathbf{h}) \\ \Im(\mathbf{W} * \mathbf{h}) \end{bmatrix} = \begin{bmatrix} \mathbf{W}^r & -\mathbf{W}^i \\ \mathbf{W}^i & \mathbf{W}^r \end{bmatrix} * \begin{bmatrix} \mathbf{x} \\ \mathbf{y} \end{bmatrix}. \quad (23)$$

Similarly, complex linear layers can be constructed using two real-valued linear ones due to the distributive property of the multiplication operator. We illustrate in Fig. 2 an example of a complex-valued NN where the weights and bias parameters of the k -th layer are $\mathbf{W}_k = \mathbf{W}_k^r + j\mathbf{W}_k^i$ and $\mathbf{b}_k = \mathbf{b}_k^r + j\mathbf{b}_k^i$, respectively. The response of this layer to an input formed from the previous layer as $\mathbf{z}^{k-1} = \mathbf{x}^{k-1} + j\mathbf{y}^{k-1}$ is given by:

$$\mathbf{z}^k = (\mathbf{W}_k^r \mathbf{x}^{k-1} - \mathbf{W}_k^i \mathbf{y}^{k-1} + \mathbf{b}_k^r) + j(\mathbf{W}_k^i \mathbf{x}^{k-1} + \mathbf{W}_k^r \mathbf{y}^{k-1} + \mathbf{b}_k^i). \quad (24)$$

Moreover, numerous activation functions have been proposed in the existing literature to handle complex-valued representations. However, in our study, we specifically employ the complex rectified linear unit (or $\mathbb{C}\text{ReLU}$). This activation function operates independently on the real and imaginary components of each complex neuron, i.e

$$\mathbb{C}\text{ReLU}(\mathbf{z}^k) = \text{ReLU}(\Re(\mathbf{z}^k)) + j \text{ReLU}(\Im(\mathbf{z}^k)). \quad (25)$$

It is important to note that there is no need to constrain the network to holomorphic functions, as it was demonstrated that ensuring differentiability of the objective function and activation functions with respect to both the real and imaginary components is a sufficient condition [34]. The training data is generated according to the model of Section II. In the case of well-separated targets, the architectures used consist of three

hidden layers and a final output layer comprising of $N_{out} = 2$ neurons corresponding to the predictions for both AoA and AoD. The input is a flattened vector of the input matrix of size $S_{inp} = N_t N_r$. The three hidden layers are mapping the input to the following latent dimensions $\left[\lfloor \frac{S_{inp}}{2} \rfloor, \lfloor \frac{S_{inp}}{4} \rfloor, \lfloor \frac{S_{inp}}{8} \rfloor \right]$. Indeed, a complex linear layer mapping \mathcal{S}_i to \mathcal{S}_o with a $\mathbb{C}\text{ReLU}$ activation function requires at total $4(\mathcal{S}_i \cdot \mathcal{S}_o) + 2\mathcal{S}_i$ multiplications and $4\mathcal{S}_o + 3\mathcal{S}_i$ additions. Consequently, we have the following total number of operations by summing the contributions of all the different layers for multiplications and additions

$$T_{\text{mul}} = 4 \left(S_{inp} \lfloor \frac{S_{inp}}{2} \rfloor + \lfloor \frac{S_{inp}}{2} \rfloor \lfloor \frac{S_{inp}}{4} \rfloor + \lfloor \frac{S_{inp}}{4} \rfloor \lfloor \frac{S_{inp}}{8} \rfloor + 2 \lfloor \frac{S_{inp}}{8} \rfloor \right) + 2 \left(S_{inp} + \lfloor \frac{S_{inp}}{2} \rfloor + \lfloor \frac{S_{inp}}{4} \rfloor + 2N_{out} \right), \quad (26)$$

$$T_{\text{add}} = 3S_{inp} + 7 \left(\lfloor \frac{S_{inp}}{2} \rfloor + \lfloor \frac{S_{inp}}{4} \rfloor \right) + 4 \lfloor \frac{S_{inp}}{8} \rfloor + 8N_{out}. \quad (27)$$

For the objective function, the MSE for the AoA is given as

$$\text{MSE}_{\text{AoA}} = \frac{1}{qE} \sum_{e=1}^E \sum_{k=1}^q \left(\widehat{\phi}_k^{\text{tar}}(e) - \theta_k(e) \right)^2, \quad (28)$$

where the same formula is used to compute the MSE for AoD using $\{\widehat{\phi}_k^{\text{tar}}(e)\}_{k,e}$. During the training process, the MSE between the estimates and true targets is minimized. This minimization allows tuning the network weights based on the gradient of the objective function. To ensure the convergence of the model, the angles $\theta_i, \phi_i, \forall i$ are sorted before computing the error, as it is necessary for the target angles to follow a deterministic order.

V. PARAMETERIZED 2D ALGORITHM

A. Algorithmic Description

Since implementing the maximum likelihood estimation is not feasible according to Section III, in this section we present a parameterized method that has knowledge of the system model of Section II, which will be used as a benchmark for the ML-based approach presented in Section IV.

Let $M_t \leq N_t$ and $M_r \leq N_r$ be the sub-array sizes. We perform a data transformation by exploiting the structure of ULA array configuration. To this end, we form $\widehat{\mathbf{H}}$ as such

$$\widehat{\mathbf{H}} = \begin{bmatrix} \widehat{\mathbf{H}}_1 & \widehat{\mathbf{H}}_2 & \dots & \widehat{\mathbf{H}}_{K_t} \\ \widehat{\mathbf{H}}_2 & \widehat{\mathbf{H}}_3 & \dots & \widehat{\mathbf{H}}_{K_t+1} \\ \vdots & \vdots & \ddots & \vdots \\ \widehat{\mathbf{H}}_{M_t} & \widehat{\mathbf{H}}_{M_t+1} & \dots & \widehat{\mathbf{H}}_{N_t} \end{bmatrix}, \quad (29)$$

where $K_t \triangleq N_t - M_t + 1$ is the number of sub-arrays formed by Tx array. Each Hankel matrix $\widehat{\mathbf{H}}_i \in \mathbb{C}^{M_r \times K_r}$ is formed as

$$[\widehat{\mathbf{H}}_i]_{m,n} = \widehat{H}_{i,m+n-1}, \quad (30)$$

where $i = 1 \dots N_t$ and $K_r = N_r - M_r + 1$ represents the number of sub-arrays formed by the receive array. Thanks to this manipulation, we can re-write equation (19) as follows

$$\widehat{\mathbf{H}} = \mathbf{A}_{M_r, M_t}(\boldsymbol{\Theta}, \boldsymbol{\Phi}) \mathbf{G} \mathbf{A}_{K_r, K_t}^T(\boldsymbol{\Theta}, \boldsymbol{\Phi}) + \widetilde{\mathbf{W}}, \quad (31)$$

$$\text{where } \mathbf{A}_{n,m}(\boldsymbol{\Theta}, \boldsymbol{\Phi}) = \begin{bmatrix} \mathbf{A}_r(\boldsymbol{\Theta})_{[1:n,:]} \\ \mathbf{A}_r(\boldsymbol{\Theta})_{[1:n,:]} \mathbf{D}_\phi(\boldsymbol{\Phi}) \\ \vdots \\ \mathbf{A}_r(\boldsymbol{\Theta})_{[1:n,:]} \mathbf{D}^{m-1}(\boldsymbol{\Phi}) \end{bmatrix}, \quad (32)$$

with $\mathbf{D}_\phi(\boldsymbol{\Phi}) = \text{diag}[\mathbf{a}_1(\phi_1) \dots \mathbf{a}_1(\phi_q)]$ and $\widetilde{\mathbf{W}}$ contains entries of $\widetilde{\mathbf{W}}$. In contrast to the model in equation (19), (31) includes interaction between both AoA and AoD within the left and right sub-spaces, due to the inflated dimensions introduced by the sub-arrays at both transmit and receive ends. Now, given (31), two overlapping matrices can be extracted from $\widehat{\mathbf{H}}$,

$$\widehat{\mathbf{H}}^{(1)} \triangleq \widehat{\mathbf{H}}_{[:,1:K_r(K_t-1)]} = \mathbf{A}_{M_r, M_t}(\boldsymbol{\Theta}, \boldsymbol{\Phi}) \mathbf{G} \boldsymbol{\Pi}^T + \widehat{\mathbf{W}}^{(1)}, \quad (33)$$

$$\widehat{\mathbf{H}}^{(2)} \triangleq \widehat{\mathbf{H}}_{[:,K_r+1:K_r K_t]} = \mathbf{A}_{M_r, M_t}(\boldsymbol{\Theta}, \boldsymbol{\Phi}) \mathbf{G} \mathbf{D}_\phi(\boldsymbol{\Phi}) \boldsymbol{\Pi}^T + \widehat{\mathbf{W}}^{(2)}, \quad (34)$$

Interestingly, both matrices can be exploited to compute $\phi_1 \dots \phi_q$. Note that for the specific matrix $\widehat{\mathbf{H}}_\gamma \triangleq \widehat{\mathbf{H}}^{(2)} - \gamma \widehat{\mathbf{H}}^{(1)}$, we have that

$$\widehat{\mathbf{H}}_\gamma = \mathbf{A}_{M_r, M_t}(\boldsymbol{\Theta}, \boldsymbol{\Phi}) \mathbf{G} (\mathbf{D}_\phi(\boldsymbol{\Phi}) - \gamma \mathbf{I}) \boldsymbol{\Pi}^T + \widehat{\mathbf{W}}_\gamma, \quad (35)$$

where $\widehat{\mathbf{W}}_\gamma = \widehat{\mathbf{W}}^{(2)} - \gamma \widehat{\mathbf{W}}^{(1)}$. In the absence of noise, and given that $\boldsymbol{\Pi}$ and $\mathbf{A}_{M_r, M_t}(\boldsymbol{\Theta}, \boldsymbol{\Phi})$ are full-column rank, the rank of $\widehat{\mathbf{H}}_\gamma$ drops from q to $q-1$ at $\gamma = \mathbf{a}_1(\phi_i), \forall i = 1 \dots q$. Based on this, one approach can be to perform an exhaustive search over ϕ as $\gamma = \mathbf{a}_1(\phi)$ and evaluate the q^{th} largest singular value of $\widehat{\mathbf{H}}_\gamma$, subsequently. Then the q minima of the resulting spectrum provide the AoD estimates. However, such an approach is computationally exhaustive as a singular value decomposition (SVD) is required per point ϕ . Instead, we perform a single SVD by first obtaining $\widehat{\mathbf{H}}^{(1)} = \mathbf{U} \boldsymbol{\Sigma} \mathbf{V}^H$, where \mathbf{U}, \mathbf{V} are the left/right singular vectors of $\widehat{\mathbf{H}}^{(1)}$ and $\boldsymbol{\Sigma}$ contains the singular values of $\widehat{\mathbf{H}}^{(1)}$ in decreasing order. Then, we truncate the SVD by first truncating $\widehat{\boldsymbol{\Sigma}} \in \mathbb{C}^{q \times q}$ by picking the upper-left $q \times q$ sub-matrix of $\boldsymbol{\Sigma}$. Similarly, $\widehat{\mathbf{U}}, \widehat{\mathbf{V}}$ are the associated singular vectors of $\widehat{\boldsymbol{\Sigma}} \in \mathbb{C}^{q \times q}$ corresponding to the q strongest singular values. Next, we compute the eigenvalues of the matrix

$$\mathbf{T} = \widehat{\boldsymbol{\Sigma}}^{-1} \widehat{\mathbf{U}}^H \widehat{\mathbf{H}}^{(2)} \widehat{\mathbf{V}}, \quad (36)$$

which are denoted as $\gamma_1 \dots \gamma_q$. These eigenvalues are estimates of $\mathbf{a}_1(\phi_i), \forall i$. Therefore, we can extract $\hat{\phi}_i, \forall i$, as follows

$$\hat{\phi}_i = -\sin^{-1} \left(\frac{\lambda \arg(\gamma_i)}{2\pi d_t} \right), \forall i = 1 \dots q. \quad (37)$$

Following the AoD estimates, we turn our attention to AoA estimation. A two-staged LS fit is proposed. The first stage entails obtaining a non-parametrized estimate of the AoA manifold via the following LS criterion.

$$\widehat{\mathbf{X}} = \arg \min_{\mathbf{X}} \left\| \widehat{\mathbf{H}} - \mathbf{X} \mathbf{A}_t^T(\widehat{\boldsymbol{\Phi}}) \right\|^2 = \widehat{\mathbf{H}} \mathbf{A}_t^*(\widehat{\boldsymbol{\Phi}}) (\mathbf{A}_t^T(\widehat{\boldsymbol{\Phi}}) \mathbf{A}_t^*(\widehat{\boldsymbol{\Phi}}))^{-1}. \quad (38)$$

The second stage exploits $\widehat{\mathbf{X}}$ to obtain a non-parametrized estimate of an un-parametrized version of $\widehat{\mathbf{A}}_r$ under a per-column norm constraint on $\widehat{\mathbf{A}}_r$. Based on this, we can write

$$(\widehat{\mathbf{A}}_r, \widehat{\boldsymbol{\alpha}}) = \begin{cases} \arg \min_{\mathbf{A}_r, \boldsymbol{\alpha}} & \|\widehat{\mathbf{X}} - \mathbf{A}_r \mathbf{G}\|^2, \\ \text{subject to} & \|\mathbf{A}_r[:,i]\| = 1, \mathbf{G} = \text{diag}(\boldsymbol{\alpha}). \end{cases} \quad (39)$$

But since \mathbf{G} is diagonal, the computation is decoupled and hence $\widehat{\mathbf{A}}_r$ can be computed on a column-by-column basis as

$$\widehat{\mathbf{A}}_r[:,i] = \begin{cases} \arg \min_{\mathbf{a}_i} & \|\widehat{\mathbf{X}}[:,i] - \alpha_i \mathbf{a}_i\|^2, \\ \text{subject to} & \|\mathbf{a}_i\| = 1, \end{cases} \quad (40)$$

where the solution can be shown to be $\widehat{\mathbf{a}}_i = \frac{\widehat{\mathbf{X}}[:,i]}{\|\widehat{\mathbf{X}}[:,i]\|}$ and $|\widehat{\alpha}_i| = \frac{\|\widehat{\mathbf{X}}[:,i]\|}{\sqrt{N_r}}$. It is worth noting that a pairing/matching method is not needed because $\widehat{\mathbf{a}}_i$ is associated with the i^{th} column of $\mathbf{A}_t(\widehat{\boldsymbol{\Phi}})$, i.e. $\mathbf{a}_{N_t}(\phi_i)$. Finally, given un-parameterized steering vectors, we perform a simple linear regression on the phases of \mathbf{a}_i to obtain the AoAs. To this end, we have the following

$$(\hat{\theta}_i, \hat{\delta}_i) = \arg \min_{\theta_i, \delta_i} \left\| \arg(\widehat{\mathbf{a}}_i) - \boldsymbol{\Xi} \begin{bmatrix} \theta_i \\ \delta_i \end{bmatrix} \right\|^2 = \boldsymbol{\Xi}^\dagger \arg(\widehat{\mathbf{a}}_i), \quad (41)$$

$\forall i = 1 \dots q$, where $\boldsymbol{\Xi} \in \mathbb{R}^{N_r \times 2}$ where the first column contains all integers counting from 1 to N_r and the second column is all-ones. It is worth highlighting that the phase offset δ_i corresponding to the i^{th} target not only contains the unknown phase of the channel coefficient (which includes the pathloss and the radar cross-section coefficient) α_i , but also the unknown phases of the transmit antenna radiation pattern due to the BS and the receive antenna radiation pattern at the radar. Therefore, its estimate, hereby denoted as $\hat{\delta}_i$ can be expressed as

$$\hat{\delta}_i = \arg(\alpha_i) + \arg(g_t(\phi_i)) + \arg(g_r(\theta_i)). \quad (42)$$

Note that the phases of $\arg(\mathbf{a}_i)$ should be unwrapped to provide a smooth phase linear estimation. We note here that in (41), one can consider replacing \mathbf{a}_i with $\widehat{\mathbf{X}}[:,i]$ since we are using the phases of \mathbf{a}_i . A summary of the algorithm is given in **Algorithm 1**.

Algorithm 1 Sensing AoA/AoD via Coarse ToA Estimates

 INPUT: $\mathbf{Y}_P, \mathbf{S}_P$

CHANNEL ESTIMATION:

 Obtain $\{\hat{\mathbf{H}}_n\}_{n=1}^{N_P}$ according to equation (13).

COARSE TIMING ESTIMATION:

- 1) For each $n = 1 \dots N_t N_r$, get $\hat{\mathbf{h}}_n$ by IFFT as in (17).
- 2) Get the q mostly occurred values in as given by (18).

SENSING ESTIMATION:

- 0) Using the \hat{i}_k -th row of $\mathbf{F}^H \hat{\mathbf{H}}^T$, form $\hat{\mathbf{H}}$ using (19).
- 1) Form $\hat{\mathbf{H}}$ as described in equations (29) and (30).
- 2) Extract $\hat{\mathbf{H}}^{(1)}$ and $\hat{\mathbf{H}}^{(2)}$ as (33) and (34), respectively.

- 3) Compute a truncated SVD of $\hat{\mathbf{H}}^{(1)}$ as

$$[\bar{\mathbf{U}}, \bar{\mathbf{\Sigma}}, \bar{\mathbf{V}}] \leftarrow \text{TSVD}_q(\hat{\mathbf{H}}^{(1)}).$$

- 4) Given $\bar{\mathbf{U}}, \bar{\mathbf{\Sigma}}, \bar{\mathbf{V}}, \hat{\mathbf{H}}^{(1)}$, compute \mathbf{T} using (36).

- 5) Get the eigenvalues of \mathbf{T} , i.e. $\{\gamma_i\}_{i=1}^q$.

- 6) For the i^{th} eigenvalue, estimate the i^{th} AoD via (37).

- 7) Perform an LS-fit following (38) to obtain $\hat{\mathbf{X}}$.

- 8) Given $\hat{\mathbf{X}}$, obtain $\{\hat{\mathbf{a}}_i\}_{i=1}^q$ through $\hat{\mathbf{a}}_i = \frac{\hat{\mathbf{X}}_{[i, :]}}{\|\hat{\mathbf{X}}_{[i, :]}\|}$.

- 9) For each i , obtain $\hat{\theta}_i$ as advised in (41).

return $(\hat{\theta}_1, \hat{\phi}_1) \dots (\hat{\theta}_q, \hat{\phi}_q)$.

B. Required Estimation Overhead & Complexity

The required estimation overheads, along with the computational complexity, required per block is explained as follows:

- **Channel Estimation**

The channel estimation step in (13) requires a series of matrix multiplications and an inverse to obtain $\hat{\mathbf{H}}_n$. A total of $N_t^2 N_P K_P + N_t^3 + N_P K_P N_t^2 + N_r N_P K_P N_t$ multiplications and $N_t(N_P K_P - 1)N_t + N_t^3 - 2N_t^2 + N_t + N_P K_P(N_t - 1)N_t + N_r(N_P K_P - 1)N_t$ additions is required to perform the channel estimation block.

- **Coarse Timing Estimation**

This block mainly performs $N_t N_r$ IFFT operations, where each consists of N_P^2 multiplications and $N_P(N_P - 1)$ additions, and hence a total of $N_P^2 N_t N_r$ multiplications and $N_P(N_P - 1)N_t N_r$ additions.

- **Sensing Estimation**

– Step 0, Step 1 and Step 2 within the sensing estimation block of **Algorithm 1** do not necessitate any floating-point operations, as we are solely arranging sub-matrices.

– Step 3 within the sensing estimation block of **Algorithm 1** performs an SVD operation, which can be realized using the Golub-Reinsch algorithm. This costs $4(M_r M_t)^2 K_r (K_t - 1) + 8M_r M_t (K_r (K_t - 1))^2 + 9(K_r (K_t - 1))^3$ multiplications and $4(M_r M_t)^2 K_r (K_t - 1) + 8M_r M_t (K_r (K_t - 1))^2 + 9(K_r (K_t - 1))^3$ additions [35], [36].

– Step 4 requires the computation of \mathbf{T} following (36), which involves the matrix multiplication of

$\hat{\mathbf{H}}^{(2)} \in \mathbb{C}^{M_r M_t \times K_r (K_t - 1)}$ with $\bar{\mathbf{V}} \in \mathbb{C}^{K_r (K_t - 1) \times q}$, which costs $M_r M_t K_r (K_t - 1)q$ multiplications and $M_r M_t (K_r (K_t - 1) - 1)q$ additions. Then, we multiply $\bar{\mathbf{U}}^H \in \mathbb{C}^{q \times M_r M_t}$ with $\hat{\mathbf{H}}^{(2)} \bar{\mathbf{V}} \in \mathbb{C}^{M_r M_t \times q}$, which costs $M_r M_t q^2$ multiplications and $(M_r M_t - 1)q^2$ additions. Finally, we multiply $\bar{\mathbf{\Sigma}}^{-1} \in \mathbb{C}^{q \times q}$ with $\bar{\mathbf{U}}^H \hat{\mathbf{H}}^{(2)} \bar{\mathbf{V}} \times \mathbb{C}^{q \times q}$. Since $\bar{\mathbf{\Sigma}}^{-1}$ is diagonal, then only q^2 multiplication are required. Therefore, we conclude that the computation of \mathbf{T} requires $M_r M_t K_r (K_t - 1)q + M_r M_t q^2 + q^2$ multiplication and $M_r M_t (K_r (K_t - 1) - 1)q + (M_r M_t - 1)q^2$ additions.

– In Step 5, we calculate the q complex eigenvalues of \mathbf{T} . Since \mathbf{T} lacks a specific structure, a QZ decomposition (generalized Schur decomposition) is suitable for generating eigenvalues, which costs $6q^2(q-1)$ multiplications, $6q^2(q-1)$ additions, and $2q(q-1)$ square roots [37]. If each square root employs coordinate rotation digital computer (CORDIC) [38], a square root operation costs $2N_{\text{cord}}$ additions and 1 multiplication, where N_{cord} is the number of iterations for the CORDIC algorithm, typically dependent on the output's bit size. Ignoring shifting operations, the overall square roots necessitate $4q(q-1)N_{\text{cord}}$ additions and $2q(q-1)$ multiplications.

– In Step 6, in order to estimate the AoD via equation (37), it is important to note that two CORDIC operations are necessary per eigenvalue. One operation is dedicated to the phase retrieval, while the other is for the inverse-sine operation. Assuming both CORDIC algorithms employ the same number of iterations as in the square root computation mentioned earlier (i.e., N_{cord}), the total number of operations needed for AoD estimation is $4N_{\text{cord}}q$ additions and $3q$ multiplications. It's worth noting that there is an additional multiplication per AoD arising from the term $\frac{\lambda}{2\pi d_t}$.

– In Step 7, the LS-fit step specified in (38) involves several computational stages. Initially, the computation of $\mathbf{A}_t^T(\hat{\Phi})\mathbf{A}_t^*(\hat{\Phi})$ requires $q^2 N_t$ multiplications and $q^2(N_t - 1)$ additions. Subsequently, the inversion of this matrix incurs q^3 multiplications and $q^3 - 2q^2 + q$ additions. Following this, the computation of $\mathbf{A}_t^*(\hat{\Phi})(\mathbf{A}_t^T(\hat{\Phi})\mathbf{A}_t^*(\hat{\Phi}))^{-1}$ necessitates $q^2 N_t$ multiplications and $N_t(q-1)q$ additions. The final step involves obtaining $\hat{\mathbf{X}}$ through the multiplication of $\hat{\mathbf{H}} \in \mathbb{C}^{N_r \times N_t}$ with $\mathbf{A}_t^*(\hat{\Phi})(\mathbf{A}_t^T(\hat{\Phi})\mathbf{A}_t^*(\hat{\Phi}))^{-1} \in \mathbb{C}^{N_t \times q}$, incurring $qN_r N_t$ multiplications and $N_r(N_t - 1)q$ additions. Consequently, the overall LS-fit operation includes $q^2 N_t + q^3 + q^2 N_t + qN_r N_t$ multiplications and $q^2(N_t - 1) + q^3 - 2q^2 + q + N_t(q-1)q + N_r(N_t - 1)q$ additions.

– In Step 9, which involves the AoA computation, we can make use of the structure of Ξ , which would then lead to a total cost of $q(N_r + 2)$ multiplications and $q(2N_r - 1)$ additions.

The computational complexity, excluding channel estimation, of **Algorithm 1** in terms of the total number of additional

TABLE I: Required Estimation Overhead (Multiplications) for Sensing AoA/AoD

Block	Complex Multiplications
Channel Estimation	$N_t^3 + 2N_P K_P N_t^2 + N_r N_P K_P N_t$
Coarse Timing Estimation	$N_P^2 N_t N_r$
Step 0, 1, 2 of Sensing Estimation	$\mathcal{O}(1)$
SVD computation (Step 3)	$4(M_r M_t)^2 K_r (K_t - 1) + 8M_r M_t (K_r (K_t - 1))^2 + 9(K_r (K_t - 1))^3$
\mathbf{T} computation (Step 4)	$M_r M_t K_r (K_t - 1)q + M_r M_t q^2 + q^2$
EVD computation (Step 5)	$2q(q - 1)$
AoD Estimation (Step 6)	$3q$
LS-fit (Step 7)	$q^2 N_t + q^3 + q^2 N_t + q N_r N_t$
Step 8	$\mathcal{O}(1)$
AoA Estimation (Step 9)	$q(N_r + 2)$

TABLE II: Required Estimation Overhead (Additions) for Sensing AoA/AoD

Block	Complex Additions
Channel Estimation	$N_t^3 - 2N_t^2 + N_t N_P K_P (N_t - 1) N_t$ $+ N_t (N_P K_P - 1) N_t + N_r (N_P K_P - 1) N_t$
Coarse Timing Estimation	$N_P (N_P - 1) N_t N_r$
Step 0, 1, 2 of Sensing Estimation	$\mathcal{O}(1)$
SVD computation (Step 3)	$4(M_r M_t)^2 K_r (K_t - 1) + 8M_r M_t (K_r (K_t - 1))^2 + 9(K_r (K_t - 1))^3$
\mathbf{T} computation (Step 4)	$M_r M_t (K_r (K_t - 1) - 1)q + (M_r M_t - 1)q^2$
EVD computation (Step 5)	$4q(q - 1)N_{\text{cord}}$
AoD Estimation (Step 6)	$4N_{\text{cord}}q$
LS-fit (Step 7)	$q^2(N_t - 1) + q^3 - 2q^2 + q + N_t(q - 1)q + N_r(N_t - 1)q$
Step 8	$\mathcal{O}(1)$
AoA Estimation (Step 9)	$q(2N_r - 1)$

and multiplications is calculated by summing up all additions and multiplications of the above sub-blocks. To this end, we have the following total number of operations

$$\begin{aligned}
 T_{\text{add}} &= 4(M_r M_t)^2 K_r (K_t - 1) + 8M_r M_t (K_r (K_t - 1))^2 \\
 &\quad + 9(K_r (K_t - 1))^3 + M_r M_t (K_r (K_t - 1) - 1)q \\
 &\quad + (M_r M_t - 1)q^2 + 6q^2(q - 1) + 4q(q - 1)N_{\text{cord}} \\
 &\quad + 4N_{\text{cord}}q + q^2(N_t - 1) + q^3 - 2q^2 + q + N_t(q - 1)q \\
 &\quad + N_r(N_t - 1)q + q(2N_r - 1)
 \end{aligned}$$

$$\begin{aligned}
 T_{\text{mul}} &= 4(M_r M_t)^2 K_r (K_t - 1) + 8M_r M_t (K_r (K_t - 1))^2 \\
 &\quad + 9(K_r (K_t - 1))^3 + M_r M_t K_r (K_t - 1)q + M_r M_t q^2 \\
 &\quad + q^2 + q^2(q - 1) + 2q(q - 1) + 3q + q^2 N_t + q^3 \\
 &\quad + q^2 N_t + q N_r N_t + q(N_r + 2)
 \end{aligned}$$

where T_{add} and T_{mul} are the total number of additional and multiplications, respectively. Comparing the complexity of the 2D parameterized algorithm with that of MLE, we first express the complexity in the order of $\mathcal{O}(N_r^3 N_t^3 q + N_r N_t q^2 + q^3)$, where we have upper-bounded both M_r, K_r by N_r and M_t, K_t by N_t . Defining the complexity gain of the parameterized method with respect to MLE as S , we can say

$$S = \frac{\mathcal{O}(G_\tau^q G_\theta^q G_\phi^q G_\alpha^{2q} (N_r N_P q^2 N_P^3 N_t + N_r N_P^2 N_P K_P))}{T_{\text{add}} + T_{\text{mul}}}. \quad (43)$$

In order to study the gains in complexity with respect to the MLE, we plot S for different values of number of targets q in Fig. 3 on a semi-log scale due to the large values involved. For a fair assessment, we have specified $G_\alpha = G_\tau = 1$ which can reflect a case where α and τ are known to the MLE. Furthermore, we set a reasonable value of $G_\phi = G_\theta = 180$, which reflects a grid of step size of nearly

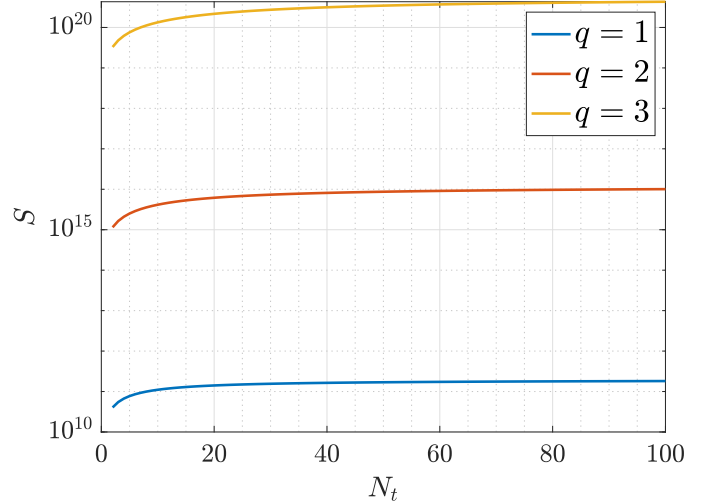


Fig. 3: The evolution of the ratio S in equation (43) for different values of N_t and q . We set $G_\tau = G_\alpha = 1$ and $G_\theta = G_\phi = 180$.

1° if the search of both AoA and AoD is from -90° to 90° . The exponential growth of values for various N_t is evident in Fig. 3. Specifically, we observe magnitudes on the order of 10^{10} for a single target and 10^{15} for $q = 2$ targets.

VI. NUMERICAL EVALUATION

In the scope of this work, we consider $N_t = 8$ transmit antennas and $N_r = 10$ receive antennas arranged in a uniform linear array (ULA) configuration with a half-wavelength spacing $\frac{\lambda}{2}$. A bandwidth of 61.44 MHz is used. The number of active subcarriers per symbol is $N_P = 64$ and the number of OFDM symbols transmitted by the BS is $K_P = 10$, assumed

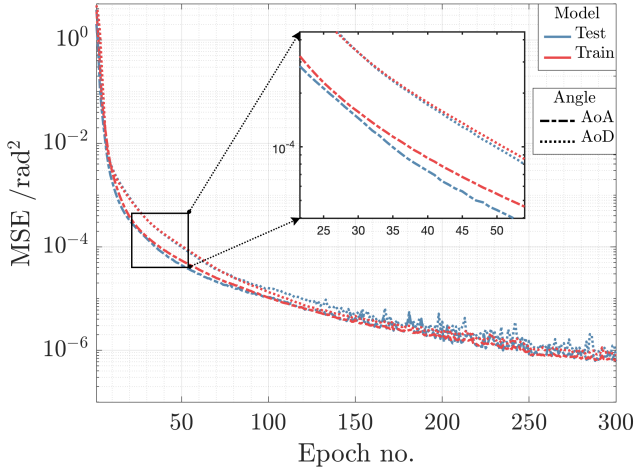


Fig. 4: Illustration of training and validation curves for AoA and AoD.

to be known at the radar unit. Both the BS and the radar unit are situated in fixed positions, while the targets are randomly positioned at varying distances, resulting in different AoA and AoD values. To capture the variability of the channel, we conduct experiments in a Monte Carlo fashion where each trial generates an independent realization of the channel. To allow duplicability of our work, the code has been made publicly available and is accessible on GitHub via the following link https://github.com/salmane-s9/Bisticat_ISAC.

A. SNR Analysis

In this section, we analyze the performance of the feed-forward network trained with different SNR values. To achieve this, we systematically train the MLP architecture using simulation data generated at specific SNRs. We then evaluate the network's performance on a test dataset with a range of SNR values from -5 to 30 dB. Our goal is to identify the optimal training strategy that maximizes the network's performance across various scenarios. For training all complex models, we employed the backpropagation algorithm along with stochastic gradient descent and Adam optimizer. The training process consists of 300 epochs, during which we assess our model's performance and investigate overfitting by analyzing the training and validation MSE losses. Fig. 4 demonstrates that both loss curves steadily decrease over the course of training, confirming effective learning and generalization to unseen data. To address overfitting concerns, we adjust the learning rate schedule, starting at $1e^{-4}$ and decreasing it by a factor of 2 at epochs 200 and 250. Fig. 5 presents the investigation of the trade-off between training the DL network on a wide range of SNRs and focusing on specific SNR values. The results clearly demonstrate the significant impact of the SNR used during training on the network's performance. Notably, the MSE is lower when evaluating the network on simulations that closely match the SNR it was trained on. Furthermore, our findings emphasize the effectiveness of training the network on a combination of simulation data with different SNR values.

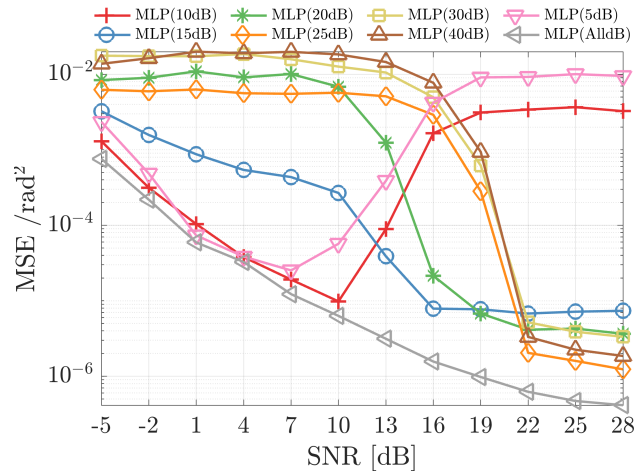


Fig. 5: Performance of the MLP architecture trained at different SNR values.

This approach enhances the network's robustness, resulting in improved performance across all SNR levels, as it is the case for the **MLP_AlldB** algorithm that was trained on a dataset with the following SNR values of $[5, 10, 15, 20, 25, 30, 40]$ dB. This can be explained by the fact that the model has effectively learned to adapt and perform well in various levels of noise associated with different SNR values. Based on these findings, we have decided to adopt a comprehensive training strategy in all our experiments. This strategy involves training the network using a combination of SNR values. It is worth noting a non-monotonic trend in the MSE results. Specifically, with a low training SNR, for instance 5 dB, the MSE initially decreases, as expected, reaching a minimum at about 5 dB, and then gradually begins to rise, eventually leveling off at approximately 10^{-2} rad² MSE. This phenomenon can be elucidated by overfitting, occurring particularly at low SNR. In such cases, the model excessively adapts to the noise, aiming to minimize MSE around the training SNR. On the other hand, when we increase the training SNR towards an acceptable range, i.e. beyond 20 dB, the overall MSE performance exhibits a more regular "waterfall" structure. Training at lower SNRs allows for a lower waterfall sensing threshold yet at the expense of a slightly lower MSE performance at higher SNRs. Interestingly, when training is conducted under a diversified set of training SNRs, i.e. 5, 10... 40 dB, the best MSE performance can be attained.

B. Performance Analysis

This section presents the performance behavior of the proposed NN architecture in comparison to the benchmark 2D estimation algorithm presented in Section V. As discussed in Section II-D, there exists a scenario where multiple paths associated with different targets may arrive within the same discrete-time delay. Consequently, the i_k -th row of the matrix $\mathbf{F}^H \mathbf{H}^T$, corresponding to the peak, is containing information about the specific targets' AoA (θ_k) and AoD (ϕ_k). Given that NN architectures require prior knowledge of targets to

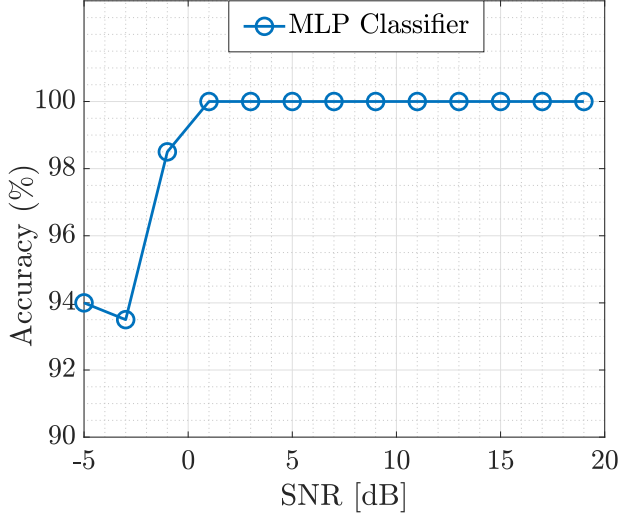


Fig. 6: Classification accuracy of the MLP model for predicting the number of targets present within a peak. The MLP classifier was trained on the following SNR values $[-10, -5, 5, 15]$ and tested on scenarios with SNRs ranging from -5 to 20 dB.

predict their directions of arrival, one of the main objectives of this analysis is to assess the MLP architecture’s capability to predict the number of targets within a peak. First, we evaluate the classification accuracy of the proposed NN by changing its output layer to softmax probabilities corresponding to the number of targets present within discrete-time delay. The results reported in Fig. 6 show that this approach can effectively help classify the presence of one or multiple targets based on the peaks in the IFFT, where the NN was trained on simulation data with different SNR values. Indeed, the classification accuracy reaches approximately 100% for SNR values greater than 0 dB. It is worth noting that we consider scenarios where at most five targets can be present in peak and therefore fixed the output size of the softmax layer to $N_{out} = 5$. Next, we compare the performance of both the convolutional and feed-forward NNs against the 2D Estimation algorithm to evaluate their ability to accurately estimate AoA and AoD in two distinct scenarios. The first case shown in Fig. 7 considers a scenario where only one target is present within a peak. The second scenario, illustrated in Fig. 8, involves two targets within the same peak. The results in both cases exhibit a good performance of the MLP algorithm compared to the 2D Estimation model, indicating its effectiveness for sensing estimation under various SNR regimes. However, it is worth noting that there is a noticeable decrease in performance for high SNR values, necessitating further investigation and potential optimization to enhance its performance in such scenarios. The CRB bound is given in Appendix A. We also observe that for a requirement of 10^{-6} MSE per radian², all methods are at about 9 dB SNR away from the CRB bound of the AoAs. This gap is due to the complexity-performance trade-off with respect to the optimal MLE estimator. The sub-optimality can be also seen

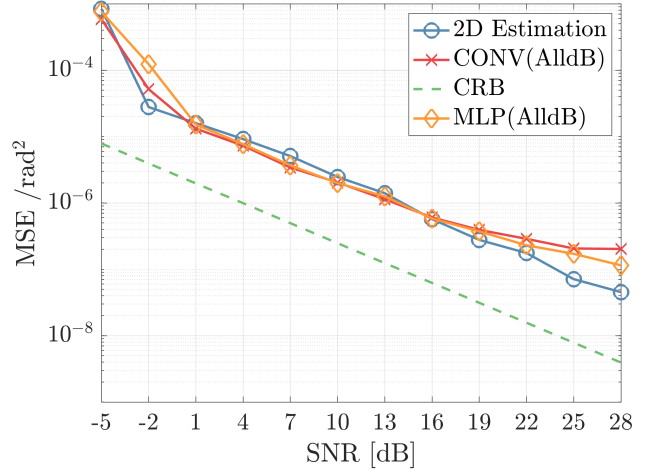


Fig. 7: Performance comparison of MLP and convolutional networks with the parametric 2D Estimation algorithm for AoA estimation.

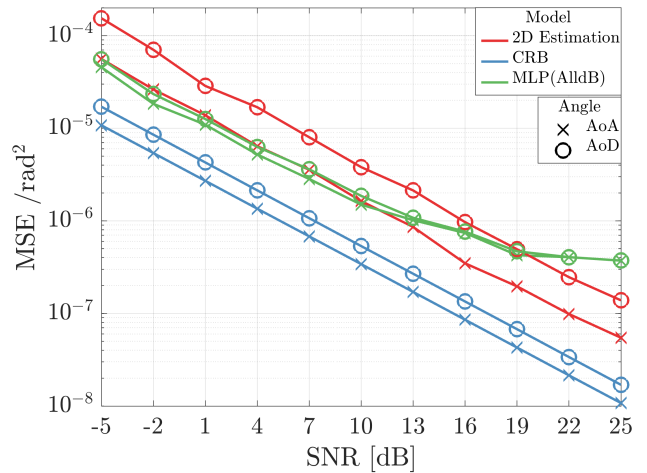


Fig. 8: Performance comparison of MLP with the 2D Estimation algorithm for both AoA and AoD angles for settings with two targets per peak.

from the timing criterion, whereby coarse estimates are being produced. Such estimates can, in turn, impact the performance at the price of reduced complexity. Moreover, notice that the MLP approach underperforms the parametric estimation one when SNR goes beyond 13 dB. The explanation posited is that when the noise level is very low, neural networks may not find it advantageous to learn more complex features, as there is already sufficient signal in the data. It is worth noting that neural networks are demonstrated to exhibit smooth functions in such scenarios. The observed saturation in the DL technique can be explained by its preference of fitting simple functions when there is enough signal. However, pushing training too far, i.e. very high number of epochs, may improve DL performance. In addition, *very deep networks* can be utilized to overcome saturation but at the cost of increased computational complexity [39].

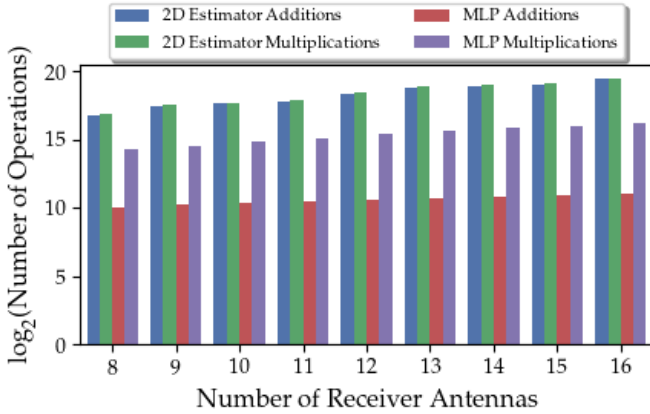


Fig. 9: Complexity comparison in terms of the number of multiplications and additions for both MLP and 2D estimation algorithm.

C. Complexity Analysis

In this section, we provide a comprehensive analysis of the computational complexity associated with joint AoA and AoD estimation using the MLP and parameterized benchmark 2D algorithm. Our focus is primarily on quantifying the number of additions and multiplications required for these estimation methods. Additionally, we highlight that our analysis does not include the complexity associated with the channel estimation and coarse timing estimation steps, as they are shared by both algorithms and are thus excluded from the analysis. Also, it is important to note that in the case of an environment with q well-resolved targets, the computational complexity reported in (26) and (27) is multiplied by a factor of q due to the increased batch size of the input, which corresponds to the number of targets present in the scene. In Fig. 9, we provide the findings of our complexity study, which show the overall number of operations required as a function of the number of receive antennas. The results are obtained for an environment with 2 targets and a fixed number of transmit antennas $N_t = 8$. As the number of receive antennas increases, we observe a slower rate of increase in the total number of operations for the MLP architecture compared to the parametric 2D estimation algorithm. Indeed, the 2D algorithm requires 6.5 and 10.3 times more multiplications than the MLP for 8 and 16 receive antennas, respectively. Therefore, the latter only requires 15.27% and 9.6% of the computational complexity required by the 2D algorithm for multiplications. This discrepancy in the rate of increase underscores the potential advantages of the MLP architecture in terms of computational efficiency and scalability, making it practical for resource-constrained scenarios. However, it is important to note that these advantages come at a trade-off with a slight degradation in performance, particularly at higher SNR values.

D. Antenna Radiation Pattern Impact

In Fig. 10, we study the impact of antenna radiation pattern on system performance, in particular the CRB. First, we use

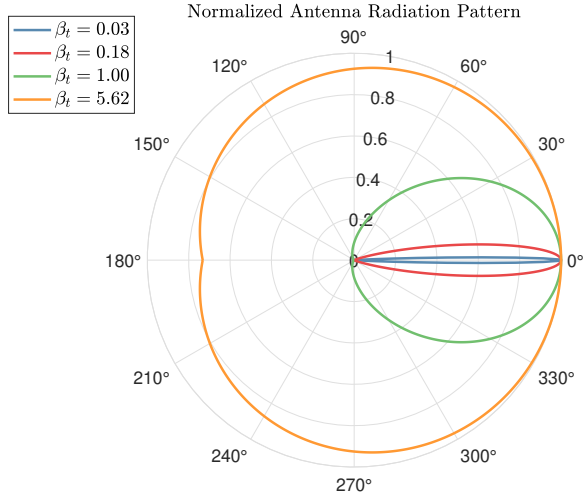
a well-known approximating antenna radiation pattern, where the main beam uses a Gaussian-like shape as [40]

$$g_t(\phi) = \Gamma_t \exp\left(\frac{-[\mathcal{M}(\phi - \phi_{t,0})]^2}{\beta_t^2}\right), \quad (44)$$

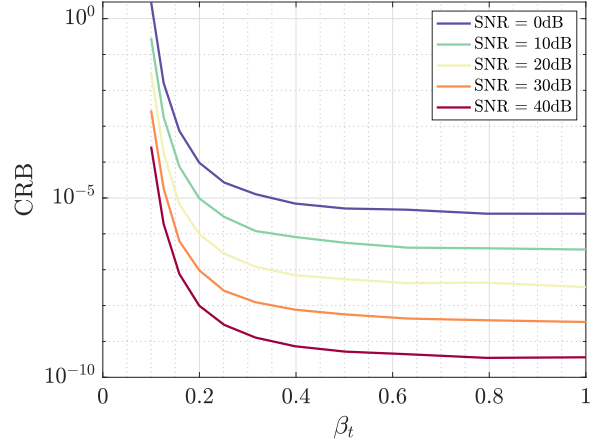
where Γ_t is scaled to reflect the transmitted power and $\mathcal{M}(\phi) = \text{mod}_{2\pi}(\phi + \pi) - \pi$ is restricted to live in $[-\pi, \pi]$. In addition, the main beam points towards $\phi_{t,0}$ and β_t specifies the beamwidth. Note that index t emphasizes that this antenna radiation pattern is dedicated for the "transmitter". Hence, a similar definition could be used to describe the antenna radiation pattern at the receiver, i.e. the radar unit. This approximation is very accurate for real practical antennas, such as those measured by leaky-wave antennas (LWAs) [41]. In fact, LWAs exhibit several distinctive advantages, including a relatively high gain, ease of fabrication, a broad bandwidth, and an inherent capability for beam scanning facilitated by a simple feed network. These attributes position LWAs as promising candidates for utilization in milli-meter wave (mmWave) applications [42]. For instance, the work in [43] designed and simulated a mmWave beam-steering LWA hexagonal patch intended for the band 24-30 GHz. In Fig. 10a, the aim is to show the resulting normalized beampattern as a function of β_t . It is clear that increasing β_t contributes to an inflation in the main beam of the antenna radiation pattern. For instance, as soon as β_t exceeds 5.6, the beampattern approaches an omni-directional structure. In Fig. 10b, we study the impact of β_t on the CRB for a single target, i.e. $q = 1$ located at $\theta_1 = 0^\circ$ and $\phi_1 = -15^\circ$. A consistent trend of the CRB can be reported for any SNR when β_t is increased. For instance, setting a CRB target performance of 10^{-5} rad^2 , the required beamwidth is $\beta_t = 0.35$ for SNR = 0 dB, whereas it is $\beta_t = 0.2$ for SNR = 10 dB, and $\beta_t = 0.15$ for SNR = 20 dB. This suggests that a more pointy beam requires higher SNR to achieve a given CRB for target sensing applications. Indeed, one can improve the performance of pointy beams by integrating a beamsteering solution, i.e. by rotating $\phi_{t,0}$ towards sectors where targets may fall in.

VII. CONCLUSION AND FUTURE WORK

In this paper, two methods for joint AoA and AoD estimation for bistatic ISAC systems are presented. One solution is a DL-based approach which leverages a complex-valued NN and incorporates a preprocessing step involving coarse timing estimation, resulting in a reduced input size and improved computational efficiency. The second method is a parameterized solution that takes knowledge of the model, which is used as a benchmark. The DL-based approach demonstrates competitive performance when compared to the parameterized method, while requiring a lower online computational complexity in terms of the number of additions and multiplications. Moreover, the DL algorithm is able to accurately estimate the number of targets whose delays arrive at the same discrete-time delay, making it suitable for dynamic environments. Nonetheless, while the performance gap with the benchmark method is generally acceptable, further research and optimization of the complex NN are necessary to enhance performance, particularly in scenarios with high SNR.



(a) Normalized beampattern ($\Gamma_t = 1$) for different values of β_t



(b) CRB as function of β_t for different SNR values

Fig. 10: Antenna radiation pattern effect on the CRB for $q = 1$ at $\theta_1 = 0^\circ$ and $\phi_1 = -15^\circ$.

It is worth noting that the existing implementations of both the DL technique and the parameterized-based method for 2D AoA and AoD estimation necessitate the re-execution of the methods whenever new target estimates are required. Recognizing this limitation, our forthcoming research endeavors will focus on the development of tracking mechanisms within both the DL and parametrized approaches. This deliberate integration is designed to simplify the process of updating AoA and AoD estimates, eliminating the requirement for sensing parameter re-estimation, especially in dynamic scenarios.

APPENDIX A CRAMÉR-RAO BOUND EXPRESSIONS

The Fisher information matrix (FIM) is given as follows

$$\mathbf{\Gamma} \triangleq \mathbb{E} \left[\frac{\partial \mathcal{L}(\boldsymbol{\xi})}{\partial \boldsymbol{\xi}} \frac{\partial \mathcal{L}(\boldsymbol{\xi})}{\partial \boldsymbol{\xi}}^T \right], \quad (45)$$

where $\boldsymbol{\xi}$ is the vector of unknown parameters, namely $\boldsymbol{\xi} = [\sigma \ \boldsymbol{\Theta} \ \boldsymbol{\Phi} \ \boldsymbol{\tau} \ \bar{\boldsymbol{\alpha}} \ \check{\boldsymbol{\alpha}}]$, where $\bar{\boldsymbol{\alpha}}$ is the real-part of $\check{\boldsymbol{\alpha}}$ and $\check{\boldsymbol{\alpha}}$ is the imaginary-part of $\bar{\boldsymbol{\alpha}}$. Furthermore, $\mathcal{L}(\boldsymbol{\xi})$ is the log-likelihood of the model, i.e. $\mathcal{L}(\boldsymbol{\xi}) = \log f(\mathcal{Y})$ and $f(\mathcal{Y})$ is the probability density function (PDF) of the observed data defined in (III). The FIM is partitioned according to the unknown variables, i.e. for any two parameter quantities, $\mathbf{\Gamma}_{\mathbf{a},\mathbf{b}} = \mathbb{E} \left[\frac{\partial \mathcal{L}(\boldsymbol{\xi})}{\partial \mathbf{a}} \frac{\partial \mathcal{L}(\boldsymbol{\xi})}{\partial \mathbf{b}} \right]$. Note that it is easy to see $\mathbf{\Gamma}_{\sigma,\sigma} = \frac{N_r N K}{\sigma^4}$ and $\mathbf{\Gamma}_{\sigma,\boldsymbol{\Theta}} = \mathbf{\Gamma}_{\sigma,\boldsymbol{\Phi}} = \mathbf{\Gamma}_{\sigma,\boldsymbol{\tau}} = \mathbf{\Gamma}_{\sigma,\bar{\boldsymbol{\alpha}}} = \mathbf{\Gamma}_{\sigma,\check{\boldsymbol{\alpha}}} = \mathbf{0}^T$. Now, denoting $\boldsymbol{\Xi}_i = \mathbf{a}_r(\theta_i) \mathbf{a}_t^T(\phi_i)$, $\boldsymbol{\Xi}_i^r = \mathbf{d}_r(\theta_i) \mathbf{a}_t^T(\phi_i)$ and $\boldsymbol{\Xi}_i^t = \mathbf{a}_r(\theta_i) \mathbf{d}_t^T(\phi_i)$, where $\mathbf{d}_r(\theta) = \frac{\partial \mathbf{a}_r(\theta)}{\partial \theta}$ and $\mathbf{d}_t(\phi) = \frac{\partial \mathbf{a}_t(\phi)}{\partial \phi}$ are the partial derivatives of the receive and transmit steering vectors with respect to θ and ϕ , respectively. In addition, we define $\check{\alpha}_i = \alpha_i g_t(\phi_i) g_r(\theta_i)$. To this end, we summarize the FIM block-matrices appearing in (45) as follows. Derivation details in what follows are omitted due to lack of space. First,

we compute all second-order partial derivatives whenever $\boldsymbol{\Theta}$ appears, i.e.

$$\begin{aligned} [\mathbf{\Gamma}_{\boldsymbol{\Theta},\boldsymbol{\Theta}}]_{i,j} &= \frac{2}{\sigma^2} \sum_{n,k} \Re \left(\mathbf{s}_{n,k}^H [\check{\alpha}_i c_n(\tau_i) \boldsymbol{\Xi}_i^r]^H [\check{\alpha}_j c_n(\tau_j) \boldsymbol{\Xi}_j^r] \mathbf{s}_{n,k} \right), \\ [\mathbf{\Gamma}_{\boldsymbol{\Theta},\boldsymbol{\Phi}}]_{i,j} &= \frac{2}{\sigma^2} \sum_{n,k} \Re \left(\mathbf{s}_{n,k}^H [\check{\alpha}_i c_n(\tau_i) \boldsymbol{\Xi}_i^r]^H [\check{\alpha}_j c_n(\tau_j) \boldsymbol{\Xi}_j^t] \mathbf{s}_{n,k} \right), \\ [\mathbf{\Gamma}_{\boldsymbol{\Theta},\boldsymbol{\tau}}]_{i,j} &= \frac{2}{\sigma^2} \sum_{n,k} \Re \left(\mathbf{s}_{n,k}^H [\check{\alpha}_i c_n(\tau_i) \boldsymbol{\Xi}_i^r]^H [\check{\alpha}_j d_n(\tau_j) \boldsymbol{\Xi}_j] \mathbf{s}_{n,k} \right), \\ [\mathbf{\Gamma}_{\boldsymbol{\Theta},\bar{\boldsymbol{\alpha}}}]_{i,j} &= \frac{2}{\sigma^2} \sum_{n,k} \Re \left(\mathbf{s}_{n,k}^H [\check{\alpha}_i c_n(\tau_i) \boldsymbol{\Xi}_i^r]^H [c_n(\tau_j) \boldsymbol{\Xi}_j] \mathbf{s}_{n,k} \right), \\ [\mathbf{\Gamma}_{\boldsymbol{\Theta},\check{\boldsymbol{\alpha}}}]_{i,j} &= \frac{2}{\sigma^2} \sum_{n,k} \Re \left(\mathbf{s}_{n,k}^H [\check{\alpha}_i c_n(\tau_i) \boldsymbol{\Xi}_i^r]^H [j c_n(\tau_j) \boldsymbol{\Xi}_j] \mathbf{s}_{n,k} \right), \end{aligned}$$

where $d_n(\tau) = \frac{\partial c_n(\tau)}{\partial \tau}$. Then, we compute all second-order partial derivatives whenever $\boldsymbol{\Phi}$ appears, i.e.

$$\begin{aligned} [\mathbf{\Gamma}_{\boldsymbol{\Phi},\boldsymbol{\Phi}}]_{i,j} &= \frac{2}{\sigma^2} \sum_{n,k} \Re \left(\mathbf{s}_{n,k}^H [\check{\alpha}_i c_n(\tau_i) \boldsymbol{\Xi}_i^t]^H [\check{\alpha}_j c_n(\tau_j) \boldsymbol{\Xi}_j^t] \mathbf{s}_{n,k} \right), \\ [\mathbf{\Gamma}_{\boldsymbol{\Phi},\boldsymbol{\tau}}]_{i,j} &= \frac{2}{\sigma^2} \sum_{n,k} \Re \left(\mathbf{s}_{n,k}^H [\check{\alpha}_i c_n(\tau_i) \boldsymbol{\Xi}_i^t]^H [\check{\alpha}_j d_n(\tau_j) \boldsymbol{\Xi}_j] \mathbf{s}_{n,k} \right), \\ [\mathbf{\Gamma}_{\boldsymbol{\Phi},\bar{\boldsymbol{\alpha}}}]_{i,j} &= \frac{2}{\sigma^2} \sum_{n,k} \Re \left(\mathbf{s}_{n,k}^H [\check{\alpha}_i c_n(\tau_i) \boldsymbol{\Xi}_i^t]^H [c_n(\tau_j) \boldsymbol{\Xi}_j] \mathbf{s}_{n,k} \right), \\ [\mathbf{\Gamma}_{\boldsymbol{\Phi},\check{\boldsymbol{\alpha}}}]_{i,j} &= \frac{2}{\sigma^2} \sum_{n,k} \Re \left(\mathbf{s}_{n,k}^H [\check{\alpha}_i c_n(\tau_i) \boldsymbol{\Xi}_i^t]^H [j c_n(\tau_j) \boldsymbol{\Xi}_j] \mathbf{s}_{n,k} \right), \end{aligned}$$

Following the above expressions, we compute all FIM partial derivatives where $\boldsymbol{\tau}$ appears

$$\begin{aligned} [\mathbf{\Gamma}_{\boldsymbol{\tau},\boldsymbol{\tau}}]_{i,j} &= \frac{2}{\sigma^2} \sum_{n,k} \Re \left(\mathbf{s}_{n,k}^H [\check{\alpha}_i d_n(\tau_i) \boldsymbol{\Xi}_i]^H [\check{\alpha}_j d_n(\tau_j) \boldsymbol{\Xi}_j] \mathbf{s}_{n,k} \right), \\ [\mathbf{\Gamma}_{\boldsymbol{\tau},\bar{\boldsymbol{\alpha}}}]_{i,j} &= \frac{2}{\sigma^2} \sum_{n,k} \Re \left(\mathbf{s}_{n,k}^H [\check{\alpha}_i d_n(\tau_i) \boldsymbol{\Xi}_i]^H [c_n(\tau_j) \boldsymbol{\Xi}_j] \mathbf{s}_{n,k} \right), \\ [\mathbf{\Gamma}_{\boldsymbol{\tau},\check{\boldsymbol{\alpha}}}]_{i,j} &= \frac{2}{\sigma^2} \sum_{n,k} \Re \left(\mathbf{s}_{n,k}^H [\check{\alpha}_i d_n(\tau_i) \boldsymbol{\Xi}_i]^H [j c_n(\tau_j) \boldsymbol{\Xi}_j] \mathbf{s}_{n,k} \right), \end{aligned}$$

Next, we compute all partial derivatives where $\tilde{\alpha}$ appears

$$\begin{aligned}\mathbf{\Gamma}_{\tilde{\alpha}, \tilde{\alpha}}]_{i,j} &= \frac{2}{\sigma^2} \sum_{n,k} \Re \left(\mathbf{s}_{n,k}^H [c_n(\tau_i) \mathbf{\Xi}_i]^H [c_n(\tau_j) \mathbf{\Xi}_j] \mathbf{s}_{n,k} \right), \\ \mathbf{\Gamma}_{\tilde{\alpha}, \tilde{\alpha}}]_{i,j} &= \frac{2}{\sigma^2} \sum_{n,k} \Re \left(\mathbf{s}_{n,k}^H [c_n(\tau_i) \mathbf{\Xi}_i]^H [j c_n(\tau_j) \mathbf{\Xi}_j] \mathbf{s}_{n,k} \right),\end{aligned}$$

Then we compute all partial derivatives where $\tilde{\alpha}$ appears

$$\mathbf{\Gamma}_{\tilde{\alpha}, \tilde{\alpha}}]_{i,j} = \frac{2}{\sigma^2} \sum_{n,k} \Re \left(\mathbf{s}_{n,k}^H [j c_n(\tau_i) \mathbf{\Xi}_i]^H [j c_n(\tau_j) \mathbf{\Xi}_j] \mathbf{s}_{n,k} \right). \quad (46)$$

Now, the CRB is obtained as follows

$$\text{CRB}(\Theta) = [\mathbf{\Gamma}^{-1}]_{2:(q+1), 2:(q+1)} \quad (47)$$

$$\text{CRB}(\Phi) = [\mathbf{\Gamma}^{-1}]_{(q+2):(2q+1), (q+2):(2q+1)} \quad (48)$$

REFERENCES

- [1] M. Chafii, L. Bariah, S. Muhaidat, and M. Debbah, "Twelve scientific challenges for 6G: Rethinking the foundations of communications theory," *IEEE Commun. Surv. Tutor.*, 2023.
- [2] F. Liu, L. Zhou, C. Masouros, A. Li, W. Luo, and A. Petropulu, "Toward Dual-functional Radar-Communication Systems: Optimal Waveform Design," *IEEE Trans. Signal Process.*, vol. 66, no. 16, pp. 4264–4279, 2018.
- [3] J. Mu, R. Zhang, Y. Cui, N. Gao, and X. Jing, "UAV Meets Integrated Sensing and Communication: Challenges and Future Directions," *IEEE Communications Magazine*, vol. 61, no. 5, pp. 62–67, 2023.
- [4] Z. Xiao and Y. Zeng, "Waveform Design and Performance Analysis for Full-Duplex Integrated Sensing and Communication," 2021.
- [5] A. Bazzi and M. Chafii, "On Outage-based Beamforming Design for Dual-Functional Radar-Communication 6G Systems," *IEEE Trans. Wireless Commun.*, pp. 1–1, 2023.
- [6] A. Bazzi and M. Chafii, "Secure Full Duplex Integrated Sensing and Communications," *IEEE Transactions on Information Forensics and Security*, vol. 19, pp. 2082–2097, 2024.
- [7] V. Kumar, M. Chafii, A. L. Swindlehurst, L.-N. Tran, and M. F. Flanagan, "SCA-Based Beamforming Optimization for IRS-Enabled Secure Integrated Sensing and Communication," in *GLOBECOM 2023 - 2023 IEEE Global Communications Conference*, pp. 5992–5997, 2023.
- [8] X. Song *et al.*, "Joint transmit and reflective beamforming for IRS-assisted integrated sensing and communication," *arXiv preprint arXiv:2111.13511*, 2021.
- [9] D. Wang, A. Bazzi, and M. Chafii, "Ris-enabled integrated sensing and communication for 6g systems," *Accepted by IEEE Wireless Communications and Networking Conference (WCNC)*, vol. 2024, Dubai, United Arab Emirates [Online]. Available: <https://arxiv.org/abs/2401.00444>, April 2024.
- [10] R. S. Thoma *et al.*, "Cooperative Passive Coherent Location: A Promising 5G Service to Support Road Safety," *IEEE Commun. Mag.*, vol. 57, no. 9, pp. 86–92, 2019.
- [11] A. Bazzi and M. Chafii, "RIS-Enabled Passive Radar towards Target Localization," *arXiv preprint arXiv:2210.11887*, 2022.
- [12] L. Leyva, D. Castanheira, A. Silva, and A. Gameiro, "Two-stage estimation algorithm based on interleaved OFDM for a cooperative bistatic ISAC scenario," in *2022 IEEE 95th Vehicular Technology Conference: (VTC2022-Spring)*, pp. 1–6, 2022.
- [13] S. Schieler *et al.*, "OFDM waveform for distributed radar sensing in automotive scenarios," *International Journal of Microwave and Wireless Technologies*, vol. 12, pp. 1–7, 07 2020.
- [14] R. Bomfin, K. S. Ali, and M. Chafii, "A System Level Analysis for Integrated Sensing and Communication," *Accepted by IEEE Wireless Communications and Networking Conference (WCNC)*, vol. 2024, Dubai, United Arab Emirates [Online]. Available: <https://arxiv.org/abs/2402.00750>, April 2024.
- [15] A. Bazzi and M. Chafii, "On Integrated Sensing and Communication Waveforms with Tunable PAPR," *IEEE Trans. Wireless Commun.*, pp. 1–1, 2023.
- [16] C. Sturm and W. Wiesbeck, "Waveform Design and Signal Processing Aspects for Fusion of Wireless Communications and Radar Sensing," *Proc. IEEE*, vol. 99, no. 7, pp. 1236–1259, 2011.
- [17] J. Fuchs, M. Gardill, M. Lübke, A. Dubey, and F. Lurz, "A Machine Learning Perspective on Automotive Radar Direction of Arrival Estimation," *IEEE Access*, vol. PP, pp. 1–1, 01 2022.
- [18] J. Fuchs, R. Weigel, and M. Gardill, "Single-snapshot direction-of-arrival estimation of multiple targets using a multi-layer perceptron," in *2019 IEEE MTT-S International Conference on Microwaves for Intelligent Mobility (ICMIM)*, pp. 1–4, 2019.
- [19] B. Milovanovic, M. Agatonovic, Z. Stankovic, N. Doncov, and M. Sarevska, "Application of neural networks in spatial signal processing (invited paper)," in *11th Symposium on Neural Network Applications in Electrical Engineering*, pp. 5–14, 2012.
- [20] M. Gall, M. Gardill, T. Horn, and J. Fuchs, "Spectrum-based Single-Snapshot Super-Resolution Direction-of-Arrival Estimation using Deep Learning," in *2020 German Microwave Conference (GeMiC)*, pp. 184–187, 2020.
- [21] G. K. Papageorgiou, M. Sellathurai, and Y. C. Eldar, "Deep Networks for Direction-of-Arrival Estimation in Low SNR," *IEEE Trans. Signal Process.*, vol. 69, pp. 3714–3729, 2021.
- [22] Z.-M. Liu *et al.*, "Direction-of-Arrival Estimation Based on Deep Neural Networks With Robustness to Array Imperfections," *IEEE Trans. Antennas Propag.*, vol. 66, no. 12, pp. 7315–7327, 2018.
- [23] J. A. Zhang, F. Liu, C. Masouros, R. W. Heath, Z. Feng, L. Zheng, and A. Petropulu, "An Overview of Signal Processing Techniques for Joint Communication and Radar Sensing," *IEEE Journal of Selected Topics in Signal Processing*, vol. 15, no. 6, pp. 1295–1315, 2021.
- [24] C. Ouyang, Y. Liu, and H. Yang, "MIMO-ISAC: Performance Analysis and Rate Region Characterization," *IEEE Wireless Communications Letters*, vol. 12, no. 4, pp. 669–673, 2023.
- [25] K. S. Ali and M. Chafii, "A Dynamic Transmission Strategy for ISAC in Large Networks," in *GLOBECOM 2023 - 2023 IEEE Global Communications Conference*, pp. 4576–4582, 2023.
- [26] A. W. Azim, A. Bazzi, R. Shubair, and M. Chafii, "Dual-Mode Chirp Spread Spectrum Modulation," *IEEE Wireless Communications Letters*, vol. 11, no. 9, pp. 1995–1999, 2022.
- [27] A. Bazzi and M. Chafii, "On Integrated Sensing and Communication Waveforms With Tunable PAPR," *IEEE Transactions on Wireless Communications*, vol. 22, no. 11, pp. 7345–7360, 2023.
- [28] F. Liu, L. Zhou, C. Masouros, A. Li, W. Luo, and A. Petropulu, "Toward Dual-functional Radar-Communication Systems: Optimal Waveform Design," *IEEE Transactions on Signal Processing*, vol. 66, no. 16, pp. 4264–4279, 2018.
- [29] S. K. Dehkordi, J. C. Hauffen, P. Jung, and G. Caire, "Hierarchical Soft-Thresholding for Parameter Estimation in Beam-Space OTFS Integrated Sensing and Communication," in *ICC 2023 - IEEE International Conference on Communications*, pp. 2939–2945, 2023.
- [30] W. Xu, Y. Xiao, A. Liu, M. Lei, and M.-J. Zhao, "Joint Scattering Environment Sensing and Channel Estimation Based on Non-stationary Markov Random Field," *IEEE Transactions on Wireless Communications*, pp. 1–1, 2023.
- [31] W. Fan *et al.*, "Antenna Pattern Impact on MIMO OTA Testing," *IEEE Transactions on Antennas and Propagation*, vol. 61, no. 11, pp. 5714–5723, 2013.
- [32] B. Friedlander, "Antenna Array Manifolds for High-Resolution Direction Finding," *IEEE Transactions on Signal Processing*, vol. 66, no. 4, pp. 923–932, 2018.
- [33] C. Trabelsi *et al.*, "Deep complex networks," *arXiv preprint arXiv:1705.09792*, 2017.
- [34] A. Hirose and S. Yoshida, "Generalization characteristics of complex-valued feedforward neural networks in relation to signal coherence," *IEEE Trans. Neural Netw. Learn.*, vol. 23, no. 4, pp. 541–551, 2012.
- [35] J. Benesty, Y. Huang, and J. Chen, "A fast recursive algorithm for optimum sequential signal detection in a BLAST system," *IEEE Trans. Signal Process.*, vol. 51, no. 7, pp. 1722–1730, 2003.
- [36] C. F. Van Loan and G. Golub, "Matrix computations (Johns Hopkins studies in mathematical sciences)," *Matrix Computations*, vol. 53, 1996.
- [37] R. C. Ward, "The combination shift QZ algorithm," *SIAM Journal on Numerical Analysis*, vol. 12, no. 6, pp. 835–853, 1975.
- [38] S. Wang and E. Swartzlander, "Merged CORDIC algorithm," in *1995 IEEE International Symposium on Circuits and Systems (ISCAS)*, vol. 3, pp. 1988–1991 vol.3, 1995.
- [39] N. Rahaman, A. Baratin, D. Arpit, F. Draxler, M. Lin, F. Hamprecht, Y. Bengio, and A. Courville, "On the Spectral Bias of Neural Networks," in *Proceedings of the 36th International Conference on Machine Learning* (K. Chaudhuri and R. Salakhutdinov, eds.), vol. 97 of *Proceedings of Machine Learning Research*, pp. 5301–5310, PMLR, 09–15 Jun 2019.

- [40] R. K. Martin and R. Thomas, "Algorithms and bounds for estimating location, directionality, and environmental parameters of primary spectrum users," *IEEE Transactions on Wireless Communications*, vol. 8, no. 11, pp. 5692–5701, 2009.
- [41] J. Werner, J. Wang, A. Hakkarainen, D. Cabric, and M. Valkama, "Performance and Cramer–Rao Bounds for DoA/RSS Estimation and Transmitter Localization Using Sectorized Antennas," *IEEE Transactions on Vehicular Technology*, vol. 65, no. 5, pp. 3255–3270, 2016.
- [42] A. Araghi, M. Khalily, P. Xiao, R. Tafazolli, and D. R. Jackson, "Long Slot mmWave Low-SLL Periodic-Modulated Leaky-Wave Antenna Based on Empty SIW," *IEEE Transactions on Antennas and Propagation*, vol. 70, no. 3, pp. 1857–1868, 2022.
- [43] M. Mantash and T. A. Denidni, "Millimeter-wave beam-steering antenna array for 5G applications," in *2017 IEEE 28th Annual International Symposium on Personal, Indoor, and Mobile Radio Communications (PIMRC)*, pp. 1–3, 2017.